# Structure of γ-secretase (PSEN1/APH-1B) in complex with Aβ46 provides insights into amyloid-β processing and modulation by the APH-1B isoform

Ivica Odorcic[1,2,3,4], Mohamed Belal Hamed Soliman[3,4], Sam Lismont[3,4], Lucía Chávez-Gutiérrez [3,4*$], and Rouslan G. Efremov[1,2*$]

[1] Center for Structural Biology, Vlaams Instituut voor Biotechnologie; Brussels, Belgium.

[2] Structural Biology Brussels, Department of Bioengineering Sciences, Vrije Universiteit Brussel; Brussels, Belgium.

[3] VIB-KU Leuven Center for Brain & Disease Research, VIB, Leuven, Belgium

[4] Department of Neurosciences, Leuven Research Institute for Neuroscience and Disease (LIND), KU Leuven, Leuven, Belgium

[*] Corresponding authors:

Lucia.ChavezGutierrez@kuleuven.be, Rouslan.Efremov@vub.be

[$] Authors jointly supervised the work.

**Abstract**

Deposition of amyloid-β (Aβ) peptides in the brain is a hallmark of Alzheimer's disease. Aβs are generated through sequential proteolysis of the amyloid precursor protein by the γ-secretase complexes (GSECs). Aβ peptide length, which is modulated by the Presenilin (PSEN) and APH-1 subunits of GSEC, is critical for Alzheimer's pathogenesis. Despite high relevance, mechanistic understanding of the proteolysis of Aβ, and its modulation by APH-1, remain incomplete. Here, we report cryo-EM structures of human GSEC (PSEN1/APH-1B) reconstituted into lipid nanodiscs in apo form and in complex with the intermediate Aβ46 substrate. We found a divergent APH-1 loop to be involved with PSEN1 in substrate-binding-induced concerted rearrangements. Upstream the catalytic site, Aβ46 structure is similar to the endopeptidase substrates and is stabilised by polar interactions including a previously unseen interaction with PSEN1 loop1. The hybrid β-sheet was not observed downstream the catalytic site.

## Introduction

Alzheimer's disease (AD), the most common form of dementia, begins with the accumulation of amyloid-β (Aβ) peptides in the brain 2-3 decades before symptoms manifest[1]. Aβ peptides of different lengths, ranging between 37 and 43 amino acids (aa), are generated by sequential cleavage of the amyloid precursor protein (APP) by the γ-secretase complexes (GSECs)[2,3]. However, it is the cerebral accumulation of longer, aggregation-prone Aβ peptides (≥ 42 aa in length) which triggers toxic molecular and cellular cascades that lead to neuronal dismissal[4].

GSECs are intramembrane multimeric proteases that cleave numerous type-I transmembrane proteins with short ectodomains and no sequence homology[5]. The ample substrate repertoire implicates GSEC activity in several biological pathways; the best characterized being Notch and APP. Processing of Notch is essential in organism development and dysregulated in cancer[6], whereas APP processing is associated with AD pathogenesis.

GSECs are constituted by presenilin (PSEN, the catalytic subunit), nicastrin (NCT), APH-1 and PEN-2[7,8]. The assembly of a tetrameric proenzyme triggers PSEN autoproteolysis and generates a pentameric active complex in which the catalytic site is formed at the interface between PSEN N- and C-terminal fragments (NTF and CTF, respectively; **Figure 1a**). In humans, the presence of two isoforms of PSEN (PSEN1, PSEN2) and two of APH-1 (APH-1A, APH-1B) generates a family of four homologous GSEC complexes[9,10] that are differentiated by distinct subcellular localisations and particular kinetics of substrate proteolysis[11,12]. GSECs containing PSEN2 and/or APH-1B subunits produce a larger proportion of longer and aggregation-prone Aβ peptides relative to those with PSEN1 and/or APH-1A subunits (**Figure 1b**)[11]. Consistently, genetic inactivation of the *Aph1B* gene in an AD mouse model reduces disease–relevant phenotypic features[13]. Recently, APH1B has been identified as an AD-risk gene in genetic studies[14].

Cleavage of APP by the β- or α-secretases[15,16] removes its large ectodomain and generates a transmembrane C-terminal fragment of either 99 or 83 aa in length ($APP_{C99}$ or $APP_{C83}$), respectively. These fragments are then proteolysed sequentially within their transmembrane (TM) domains by GSEC: a first endopeptidase-like cut at position 48 or 49 releases the APP intracellular domain (AICD). Next, the resulting substrate is proteolysed by three to four residues at a time by several sequential carboxypeptidase-like cuts[2,3,17] (**Figure 1b**). Every cut lowers the stability of the successive enzyme-substrate (E-S) complexes[18] until Aβ40, or Aβ42/Aβ38 in the other product-line, is released to the extracellular/luminal environment. Consistently, mutations in PSEN that destabilise GSEC-APP/Aβ interactions enhance production of the longer and more hydrophobic Aβ42 and Aβ43 peptides[18] and cause early-onset familial AD (FAD)[19].

Recent cryo-EM structures of GSEC (PSEN1/APH-1A) in complex with $APP_{C83}$[20] or Notch[21] substrates revealed that E-S complex formation is associated with substantial conformational rearrangements in both enzyme and substrate to reach remarkably similar structures of the complexes, despite the low sequence homology between these substrates. In both structures, the transmembrane region of substrate unwinds close to the scissile bond and forms a hybrid substrate-GSEC β-sheet structure. The latter is suggested to be essential element of substrate stabilisation.

Despite the wealth of structural information on GSEC, the mechanistic basis of GSEC processivity (sequential cleavage) and its modulation by isoforms of the APH-1 subunit remains unknown. Importantly, enzyme processivity is regulated at the level of GSEC-$Aβ_n$ interactions; however, only the structures of GSEC with the initial endopeptidase APP/Notch substrates are known.

Here, we report the cryo-EM structures of GSEC (PSEN1/APH-1B, referred to as GSEC1B) complexes in apo form and in complex with the intermediate Aβ46 substrate in a native-like environment and in the absence of E-S cross-linking. Structural comparison with GSEC1A (PSEN1/APH-1B) shows concerted isoform-dependent structural changes at the active site (PAL motif; PSEN1 Pro433-Leu435) and at the PSEN-1/APH-1 interface, upon substrate-binding. This provides structural understanding of the involvement of the APH-1 subunit in substrate gating/processing in an isoform-dependent manner.

The GSEC-Aβ46 structure shows conservation of H-bonding interactions between GSEC and initial/intermediate substrates, while functional studies establish their contribution to substrate stabilisation and processing. Taken together, these findings indicate that the substrate backbone structure is remarkably preserved during sequential proteolysis.

## Results

### Cryo-EM structure determination

We characterised the GSEC1B isoform in apo form and in complex with the Aβ46 peptide using cryo-EM single particle analysis. Aβ46 is generated during the sequential (carboxypeptidase-like) cleavage of APP and is hydrolysed to the major Aβ40 product (**Figure 1b)**. We purified human GSEC1B from High Five insect cells[11] and reconstituted it into lipid nanodiscs to more closely mimic the membrane environment[22]. Screening for reconstitution conditions established that the combination of membrane scaffold protein (MSP) MSP1D1 and a 1:2 (M/M) POPC:DLPC lipid mixture produced homogeneous GSEC nanodiscs suitable for high-resolution cryo-EM (**Figure 1c, d** and **Extended Data Figures 1-4**).

Previous structural analyses of GSEC in complex with its substrates have generated high resolution data for the interaction with the initial endopeptidase substrates $APP_{C83}$[20] and Notch[21]. To gain insights into GSEC-substrate interactions during carboxypeptidase-like cleavages, we generated an inactive GSEC1B enzyme, containing a catalytically inactive but mature PSEN1 D275A mutant (pentameric $GSEC1B^{D275A}$), in complex with Aβ46 (**Figure 1c, d**). Incubation of Aβ46 with the reconstituted wild type GSEC1B complex resulted in generation of Aβ40 (**Figure 1e**), while the reconstituted $GSEC1B^{PSEN1\ D257A}$ mutant did not hydrolyse Aβ46 (**Figure 1e**). However, the latter formed stable E-S complexes (see below). The inspection of cryo-EM samples of GSEC1B on holey grids revealed that more than 90% of particles were fragmented, likely because of interaction with the air-water interface[23,24]. This difficulty was overcome by using high-coverage graphene oxide-coated grids, utilising a refined protocol relying on poly-L-lysine pre-coating[25] (Materials and Methods). To improve particle orientation distribution, the graphene oxide surface was coated with polyethylene glycol (PEG). Similar conditions were applied to reconstruct the structure of the $GSEC^{PSEN1\ D257A}$-Aβ46 complex (**Extended Data Figures 2 and 4**).

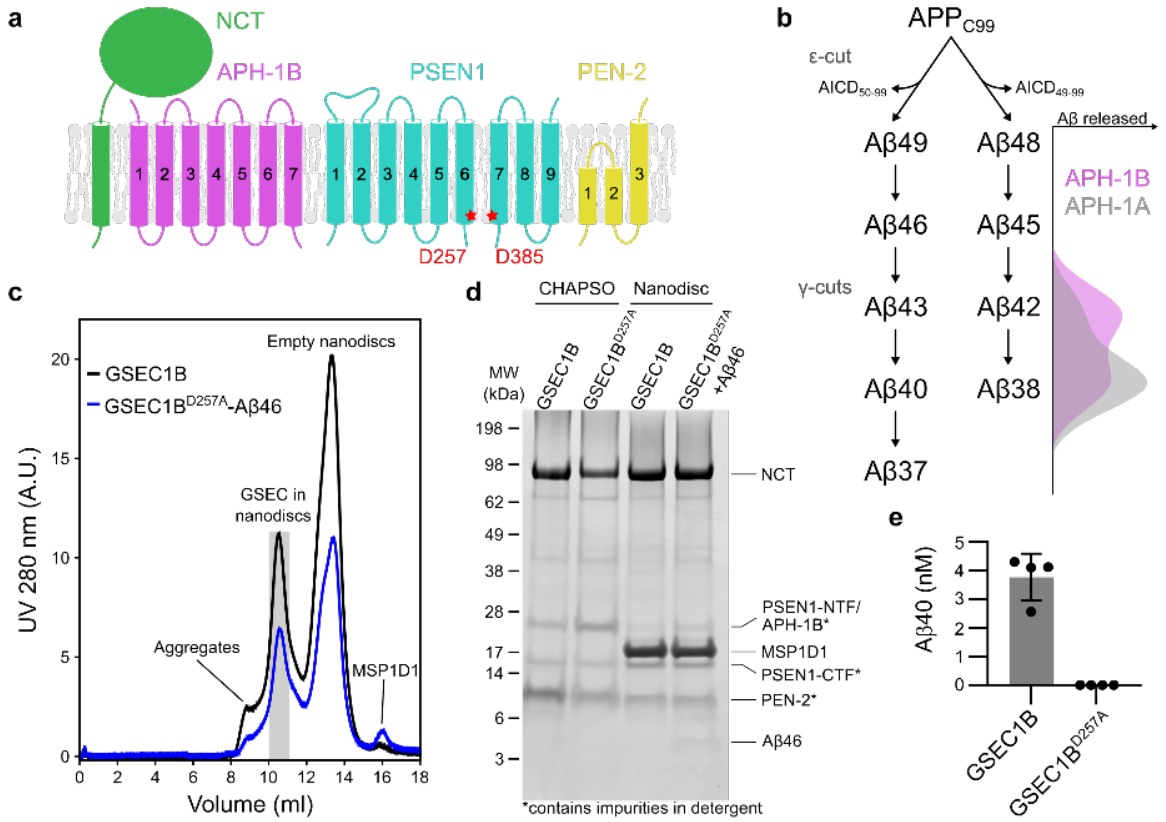


**Figure 1. Reconstitution of GSEC1B into lipid nanodiscs. a,** Schematic representation of GSEC subunits. The catalytic aspartates are indicated, and their respective positions are marked with red stars. **b,** Sequential processing of APP$_{C99}$ by GSEC. The difference in processivity between the APH-1 isoforms is indicated. **c,** Size exclusion chromatograms of GSEC1B and GSEC1B$^{D257A}$-Aβ46 after reconstitution into MSP1D1 lipid nanodiscs. Grey area shows peak fraction used for cryo-EM. **d,** Coomassie stained SDS-PAGE of purified GSECs (wild-type and D257A mutant) solubilised in CHAPSO and reconstituted into lipid nanodiscs. Aβ46 was added to the purified GSEC$^{D257A}$ prior to reconstitution. **e,** ELISA-based quantification of Aβ40 generated from Aβ46 by GSEC1B solubilised in CHAPSO or reconstituted into lipid nanodiscs. Averages of 4 independent measurements and standard deviation are shown.

## Structure of apo GSEC1B

We solved the structure of GSEC1B in lipid nanodiscs to an overall resolution of 3.3 Å (**Figure 2a, b, Table 1, and Extended Data Figures 1, 2**). The map was of sufficient quality to model 68% (or 1224 residues) of the structure (**Supplementary Table 1**). The subunits NCT, APH-1B and PEN-2 were modelled almost entirely, whereas around half of the encoded polypeptide was modelled for PSEN1. Specifically, loop 1 (residues 103-124, connecting TM1-TM2), TM2, part of TM6, and the large intracellular loop between TM6-TM7, except for a 9-residue stretch preceding the autoproteolytic cleavage site (Glu280-Ser289), were not resolved in PSEN1. Three elongated densities in the membrane-embedded region at the interfaces between TM1,8$^{PSEN1}$ and TM4$^{APH-1B}$; TM1,4,7$^{APH-1B}$ and NCT$^{TM}$; and TM5,7$^{APH-1B}$ were modelled as phospholipids (**Figure 2a, b**). The latter replaces a cholesterol moiety reported in digitonin solubilised GSEC1A structures[20,21,26,27].

Structural comparison of GSEC1B with the apo state model of human GSEC1A solved in amphipols[28,29] showed a high overall similarity (RMSD of 1.2 Å over 7918 atoms; **Figure 3a, Supplementary Table 2, Supplementary Video 1**). Nevertheless, the transmembrane region of GSEC1B was expanded by ~ 2 Å as compared to GSEC1A (**Supplementary Video 1**).

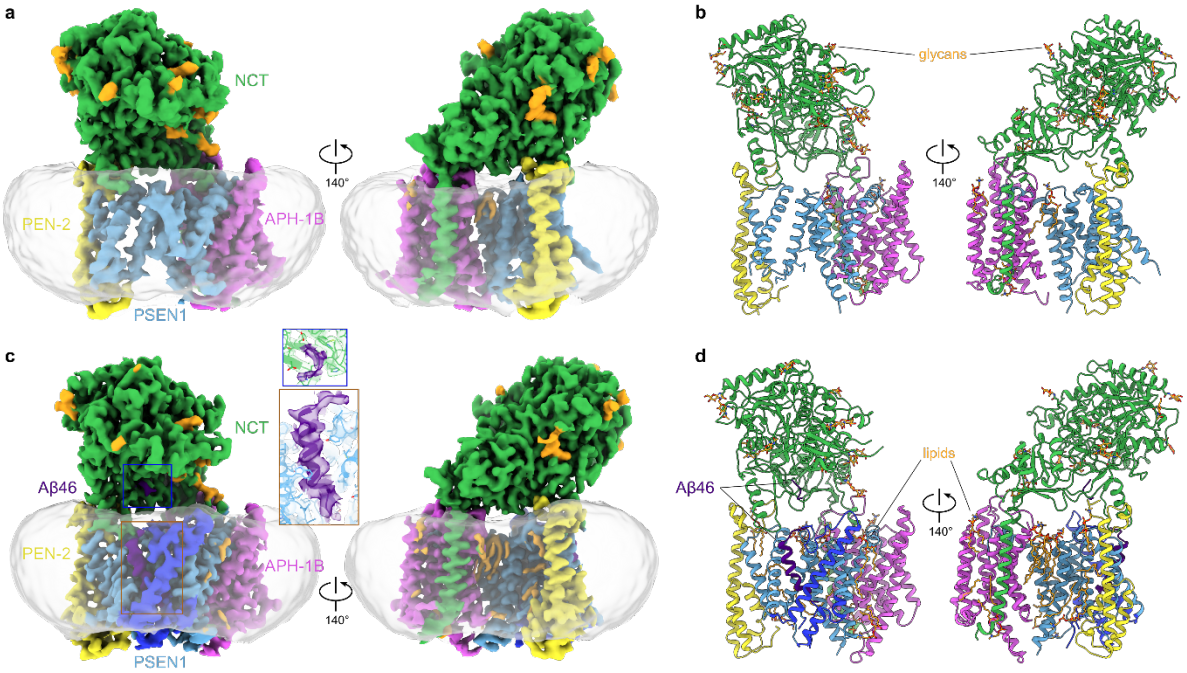


**Figure 2. Cryo-EM structures of GSEC1B and GSEC1B-Aβ46 complex in lipid nanodiscs. a,** Cryo-EM map of apo GSEC1B coloured by subunit. Resolved glycans in NCT subunit and density corresponding to ordered lipids are coloured in orange. The density corresponding to lipid nanodisc extends ~ 2 nm around the edge of GSEC and is ~ 4 nm thick, with the thickest part found next to PEN-2, and the thinnest part close to APH-1B. **b,** Atomic model of apo GSEC1B. **c,** Cryo-EM density map of GSEC1B-Aβ46 complex, Aβ46 shown in purple. Regions of PSEN1 resolved in the complex with Aβ46 but not in apo state are shown in dark blue. Density of Aβ46 N-terminus proximal to $Glu650^{NCT}$ and of the density of Aβ46 TM domain are shown in the inset. The maps shown in panels **a** and **c** were filtered using Gaussian filter for better visualisation. **d,** Atomic model of the GSEC1B-Aβ46 complex.

To gain insights into the APH-1 isoform-dependent allosteric-like effects, we analysed the structural differences between APH-1A and APH-1B subunits. In humans, subunits APH-1A and APH-1B share a 56% sequence identity with mostly conservative substitutions scattered throughout their sequence (**Figure 3b, e**). Despite the very similar overall structures (RMSD of 0.9 Å over 1283 atoms) the backbones of the isoforms diverged locally at three segments on the inner and outer membrane surfaces, with changes mapping to the PSEN1/APH-1 interface (**Figure 3a, b**). Specifically, the extracellular ends of TM2-TM3 and TM6-TM7 helical pairs were bent by 4° and 7°, respectively; whereas the cytosolic TM3-TM4 connecting loop (residues 104-110) was partially disordered in APH-1B but resolved in APH1-A. Notably, these structural differences coincide with local clusters of sequence divergence between the APH-1 isoforms (**Figure 3e**).

To get further insight into a possible APH-1 isoform-driven allosteric-like mechanism, we examined the PSEN1/APH-1 interface. This interface spans an area of ~2000 $Å^2$ and involves the interaction between adjacent α-helices of APH-1 (TM2-TM4) and PSEN1 (TM1, TM8-TM9) as well as the insertion of the PSEN1 C-terminus into the APH-1 helical bundle on the extracellular side (**Figure 3c**). The interactions between PSEN1 and APH-1 are conserved between the isoforms, except for: four substitutions in the transmembrane helices (APH-1B/APH-1A: I32/V32, I36/V36, L51/V51 and M127/I128; **Figure 3d**) and several substitutions in the pocket where the PSEN1 C-terminus binds (APH-1B/APH-1A: N62R, K69Y, T136I, F155Y, Y159T, M162L, V199T, S206N; **Supplementary Table 3**). We speculated that despite the overall structural similarity, differences in length, charge and/or polarity of the side chains forming the PSEN1/APH-1 interface (**Supplementary Table 3)**

might alter enzyme dynamics or its structure when the substrate binds, thus leading to the observed functional effect**.**

Significant conformational differences between GSEC1A and GSEC1B structures in apo states are observed in the catalytic PSEN1 subunit. In the active site of PSEN1, the TM8-TM9$^{PSEN1}$ loop containing the conserved and functionally important PAL motif[30] is resolved in GSEC1B, but not in GSEC1A. The cytoplasmic end of TM8$^{PSEN1}$ interacts with APH-1A but bends away from APH-1B by ~16°, suggesting that the difference in its dynamics might be linked with APH-1 isoforms. Moreover, the cytoplasmic end of TM6$^{PSEN1}$ (between the catalytic Asp257 and Pro264) and the first helical turn of TM7$^{PSEN1}$ (Val379-Gly382) were structured in GSEC1A but unresolved in GSEC1B. In the latter, the volume of the ordered cytoplasmic end of TM6$^{PSEN1}$ (Leu258-Pro264) in GSEC1A is occupied by the TM8-TM9$^{PSEN1}$ loop. In addition, the PSEN1 Glu280-Ser289 fragment of the long intracellular TM6-TM7 loop (residues 278-382) is resolved at the interface between PSEN1 TM3 and TM7 only in GSEC1B structure (**Figure 3a**) where it occupies the same position as in the substrate-bound GSEC1A structures[20,21]. Lastly, the cytoplasmic end of TM3 is extended by two helical turns (K160-L166) in GSEC1B, relative to GSEC1A (**Figure 3a**). The observed conformational differences in the PSEN1 subunit may arise from the interaction with different APH-1 isoforms and/or from the different lipid mimetic environments (nanodiscs versus amphipols) used to solve the structures of the complexes.

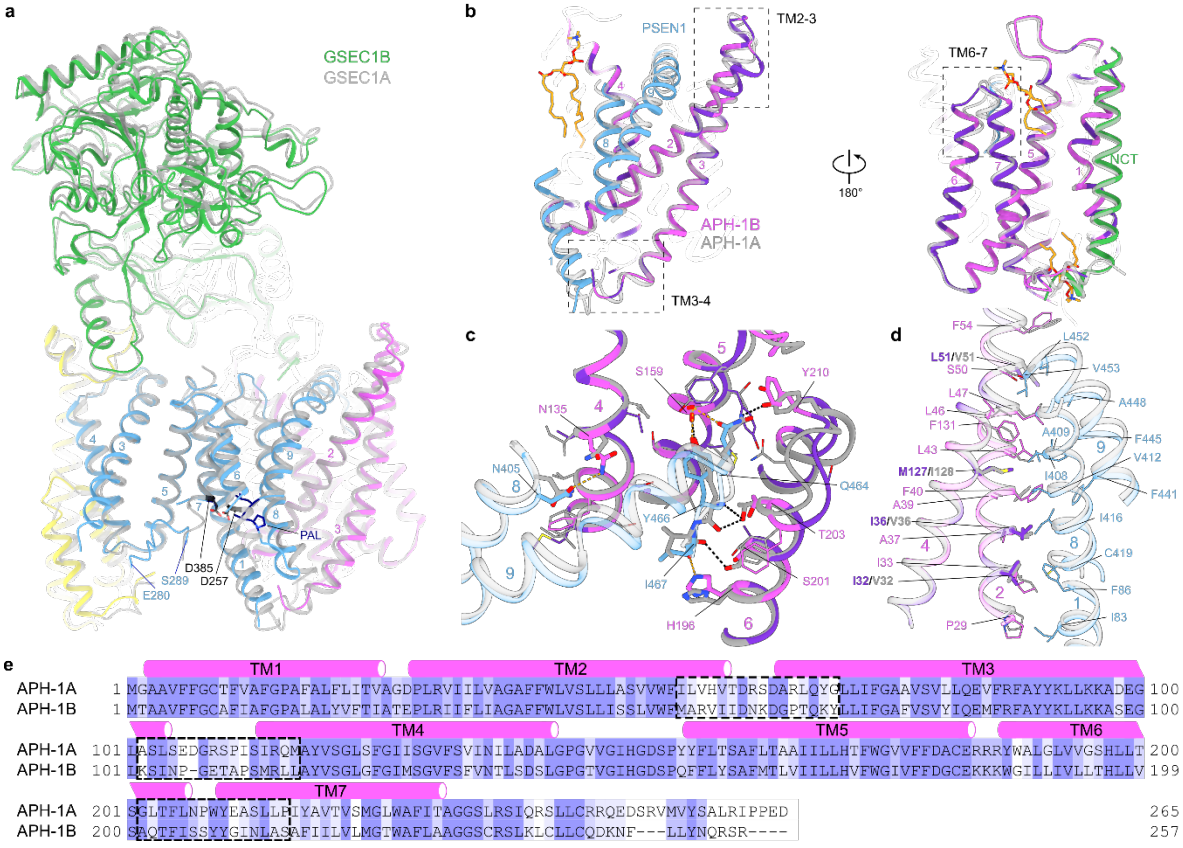


**Figure 3. Structural differences at the PSEN1/APH-1 interface. a**, Structural comparison of GSEC1B and GSEC1A (PDB: 5FN5). GSEC1B is colour coded as in Figure 2, GSEC1A is shown in grey. The sidechains of the catalytic aspartates and the PAL motif are shown as sticks. **b**, Structural differences between APH-1 isoforms. Residues that differ between the isoforms are coloured in purple. **c**, Details of the interfaces between C-terminus of PSEN1 and APH-1 isoforms. Putative hydrogen bonds between PSEN1 and APH-1B are shown in orange, and hydrogen bonds between PSEN1 and APH-1A are shown in black. **d**, Details of the transmembrane PSEN1/APH-1 interface. **e**, Sequence

alignment of human APH-1A and APH-1B. Positions of TM helices are indicated graphically. Dashed boxes in **b** and **e** indicate regions displaying significant structural differences.

## Structure of GSEC1B-Aβ46 complex

We next investigated GSEC-Aβ interactions and the role of APH-1 isoforms in substrate processing by determining the GSEC1B structure in complex with Aβ46. For structural analysis, the inactive GSEC1B$^{D257A}$ mutant was reconstituted into lipid nanodiscs in the presence of Aβ46 (**Figure 1c, d**) and supplemented with an excess of Aβ46 prior to plunge freezing the cryo-EM grids. The reconstituted GSEC1B-Aβ46 complex was sufficiently stable for structural analysis without the need for crosslinking, a strategy previously used for stabilisation of GSEC-substrate complexes[20,21].

Extensive 3D classification, after partial signal subtraction, enabled the isolation of a uniform population of GSEC1B-Aβ46 complexes and their reconstruction to a resolution of 3.4 Å (**Figure 2c, d, Table 1, and Extended Data Figures 3, 4**). In the presence of substrate, parts of PSEN1 disordered in apo became resolved; we modelled 73% of the GSEC1B sequence (**Supplementary Table 1**), including a 24-residue-long continuous Aβ46 fragment. A total of 14 boundary phospholipids were also modelled in the map (**Figure 2c, d**).

Aβ46 binding triggered substantial structural rearrangements within the catalytic subunit (**Figure 4 and Supplementary Video 2**) that are similar to those previously reported[20,21]. Nevertheless, specific structural differences between the initial endopeptidase substrates and intermediate Aβ46 are observed in functionally relevant regions in PSEN1 (**Figure 5 a-c**) (see below).

The PSEN1 subunit has high similarity (RMSD of 0.6 Å) in all three (Aβ46/APP$_{C83}$/Notch[20,21]) substrate-bound structures. When compared to the apo state, the changes in PSEN1 include: ordering of TM2, adjacent loop 1 and intracellular extensions of TM6 and TM7 (**Figure 2c, d and Figure 4**; dark blue); bending of TM1; shifts of TM3 and TM6 by ~5 Å, relative to the substrate; and shift of the PAL motif containing loop by 3.4 Å toward the substrate (**Figure 4 and Supplementary Video 2**).

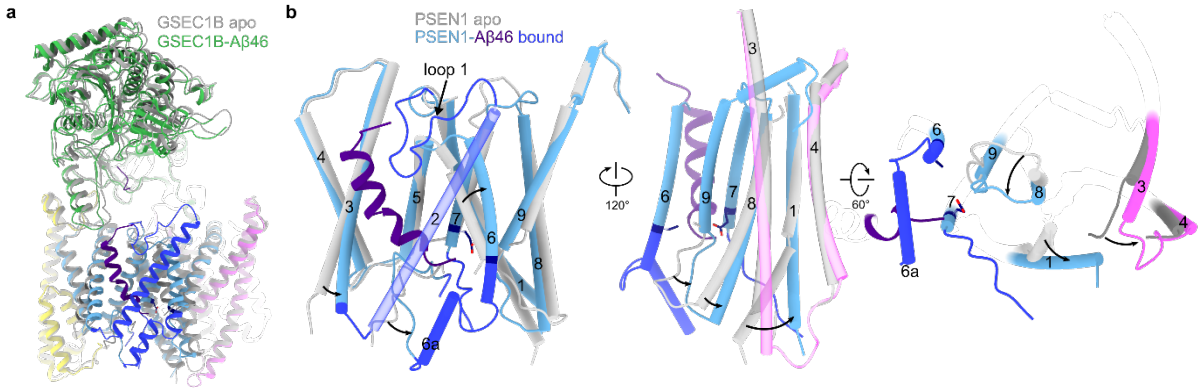


**Figure 4. Conformational changes between apo and Aβ46-bound GSEC1B. a,** Structural alignment of apo and Aβ46-bound GSEC1B. **b**, Structural rearrangement in PSEN1 and APH-1 subunits upon Aβ46 binding.

Our structures allowed a direct comparison of apo versus substrate-bound states in a native-like environment. They showed that substrate-induced conformational changes in PSEN1 propagate into a divergent region in the APH-1 isoforms (TM3-TM4 loop) (**Figure 4b and Supplementary Figure 5a**). An apparent allosteric-like pathway links TM8-9$^{PSEN1}$ loop with the extracellular end of TM1$^{PSEN1}$ which in turn interacts with the TM3-TM4$^{APH-1}$ loop. The

sequence, structures, length and charges of TM3-TM4$^{APH-1}$ loop are different between GSEC1A and GSEC1B with bound substrate (**Figure 3e, Supplementary Figure 5a**).

The conformations of TM1$^{PSEN1}$, which links active site TM8-TM9$^{PSEN1}$ loop with APH-1, are similar between the substrate-bound structures of GSEC1A and GSEC1B suggesting that the structural differences alone cannot account for the observed allosteric-like effect on APH-1 isoforms. However, TM1$^{PSEN1}$ is highly dynamic. Upon substrate binding, it shifts vertically by ~ 1.5 Å towards the extracellular side, supporting the notion that piston-like movement of TM1$^{PSEN1}$ is associated with activity[31,32]. Furthermore, its intracellular end bends by 33° towards APH-1 at Pro88 which functions as a hinge. FAD-causing P88L mutation which interferes with TM1$^{PSEN1}$ dynamics strongly impairs processivity[33,34]. In a similar manner, APH-1 isoforms might change the environment of TM1$^{PSEN1}$ and modulate GSEC processivity.

The density of the Aβ46 substrate was well-resolved for the backbone (**Figure 6b, Extended Data Figure 3**), but did not allow the assignment of sequence register with confidence, hence, we modelled it as a polyalanine chain. We note that the sequence of the membrane-embedded fragment of Aβ46 does not contain bulky aromatic residues but does include structural signature features, such as residues with long and branched side chains as well as a tandem of glycines (**Figure 6c**). We interpret the lack of clear side-chain densities as the superposition of Aβ46 peptides bound with different registers (positions within the binding channel).

**Structural and functional determinants of GSEC-Aβ46 interaction**

The comparison of the GSEC1A-APP$_{C83}$[20] with GSEC1B-Aβ46 complexes showed that the backbones of the substrates closely overlap in the transmembrane region (RMSD of 1 Å over 85 atoms, **Figure 5a-d**), but deviate at the extracellular and cytoplasmic interfaces.

On the extracellular side, and similar to other substrate-bound structures[20,21], an additional density consistent with the bound N-terminus of Aβ46 is observed close to Glu650 on the surface of the NCT ectodomain (**Figure 2c**). Furthermore, the backbone of the extracellular juxtamembrane region of Aβ46 forms a short, extended strand that bends over loop 1 (**Figure 5a-b**). This feature contrasts with the straight helical conformation of the backbones of APP$_{C83}$[20] and Notch[21] in this region. When compared with APP$_{C83}$, the backbone of the first common α-helical turn of Aβ46 bends by about 2.2 Å towards loop 1 (**Figure 5a**). This relative shift appears to be the result of the pronounced conformational differences in loop 1, relative to the cross-linked GSEC-APP$_{C83}$/Notch structures which were obtained using a Q112C PSEN1 and Notch/APP$_{C83}$ P1728C/V695C mutants (**Figure 5a-b, d and Supplementary Video 3**).

Loop 1 regulates GSEC proteolysis, mediates the binding of allosteric GSEC modulators, and harbours 23 FAD-linked pathogenic mutations (https://www.alzforum.org/mutations/psen-1, accessed on 28 June 2023). In the GSEC1B-Aβ46 complex, the tip of loop 1 (Tyr115) is inserted 4.5 Å deeper into the substrate-binding transmembrane channel and points towards Aβ46 (**Figure 5a-b, d**), such that the hydroxyl group of Tyr115$^{PSEN1}$ is positioned ~ 4.7 Å from the substrate backbone and reaches approximately the middle of the bilayer (**Figure 5b, d**). To investigate a possible interaction, we mutated Tyr115$^{PSEN1}$ to Phe and Ala, and rescued (wild-type or mutant) PSEN1 expression in PSEN1/PSEN2 deficient cells. The presence of mature, glycosylated NCT and N- / C-terminal fragments of PSEN1 demonstrated the efficient reconstitution of GSEC complexes in all generated cell lines (**Figure 5e**). To determine the effects of these substitutions in PSEN1 on APP processing, we transiently expressed the APP$_{C99}$ substrate in the WT/mutant cell lines and measured secreted Aβ 37/38/40/42 peptides in the conditioned media by ELISA. Removal of either the hydroxyl group (Tyr to Phe mutation) or the aromatic ring of Tyr115 (Tyr to Ala mutation) shifted the short-to-long

Aβ (37+40+38)/(43+42) peptide ratio (**Figure 5f**). Because this ratio provides an estimation of GSEC processivity[35], the decrease points towards the involvement of Tyr115$^{PSEN1}$ in hydrogen bonding and Van der Waals interactions that stabilise the GSEC-Aβ complex during its sequential cleavage.

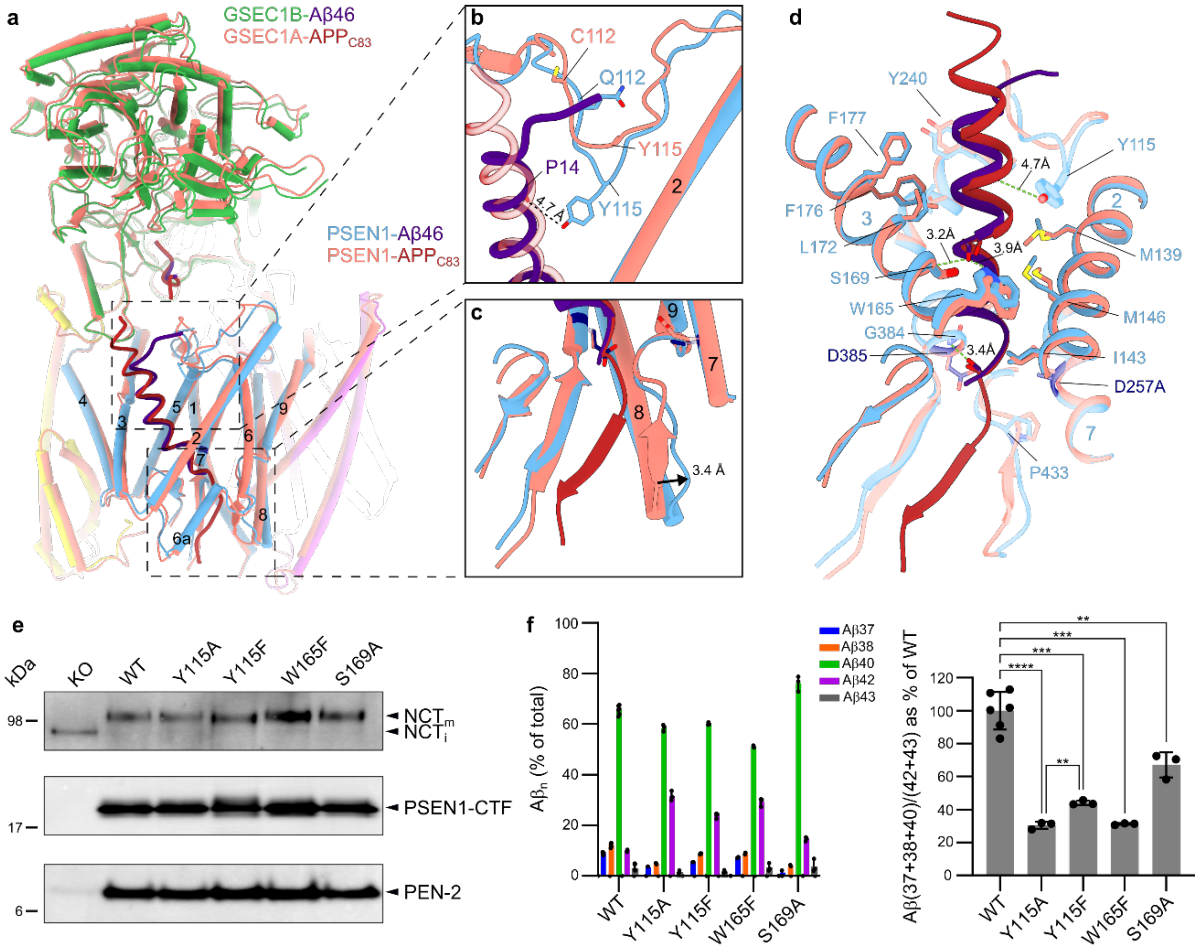


**Figure 5. Structural comparison of GSEC1B-Aβ46 with GSEC1A-APP$_{C83}$ and experimental validation of potential hydrogen bonds between PSEN1 and APP. a,** Structural alignment of GSEC1B-Aβ46 and GSEC1A-APP$_{C83}$ (PDB: 6IYC; shown in grey) complexes. **b,** Closeup of extracellular side of the substrate and loop 1. The GSEC1A-APP$_{C83}$ complex was stabilised by disulphide crosslink between V7C APP$_{C83}$ (unresolved) and Q112C PSEN1. **c**, Closeup view on intracellular side of substrate binding site. **d**, Details of PSEN1-Aβ46 interactions in the trans-membrane region. Potential hydrogen bond interactions between the substrates and W165, S169 and G384 are indicated. **e,** Western blot analysis of solubilised membranes from *Psen1$^{-/-}$/Psen2$^{-/-}$* (dKO) mouse embryonic fibroblast cell lines rescued with WT or mutant PSEN1. NCT$_m$ and NCT$_i$ indicate mature glycosylated and immature NCT, respectively. Molecular weights of protein standards are indicated on the left. **f**, GSEC processivity of APP$_{C99}$ in *Psen1$^{-/-}$Psen2$^{-/-}$* MEFs rescued with WT or mutated PSEN1. Data are presented as mean ± SD, N ≥ 3. Multiple comparison ANOVA was used to determine statistical significance (P < 0.05); ** P < 0.01, *** P < 0.001, **** P < 0.001.

In the extracellular leaflet, the TM domain of Aβ46 adopts an α-helical conformation, with three helical turns partially exposed to lipids and partially to PSEN1. Starting from the 4$^{th}$ turn, similar to the structures of APP$_{C83}$/Notch[20,21] Aβ46 is enclosed by PSEN1, its helical pitch elongates and transitions to an extended strand conformation (**Figure 5d, Figure 6a**). Notably, the disrupted intra-helical hydrogen bonds within the Aβ46/APP$_{C83}$/Notch substrates are compensated by interactions with hydrogen-donor side chains in PSEN1: Ser169 and Trp165

(**Figure 5d**). The contribution of these interactions to the stability of enzyme-substrate interactions, and therefore GSEC processivity[18], remains unknown.

To assess their functional relevance, we generated W165F and S169A PSEN1 mutants that are unable to form hydrogen bonds and stably expressed them in PSEN1/PSEN2 deficient cells. Western blot analysis of NCT maturation and PSEN1 endoproteolysis showed that both mutants efficiently reconstituted mature GSEC complexes (**Figure 5e**), while the ELISA-based analysis of secreted Aβ profiles demonstrated that these mutations impaired GSEC processivity of $APP_{C99}$. These results support the involvement of both residues in Aβ substrate stabilisation (**Figure 5f**).

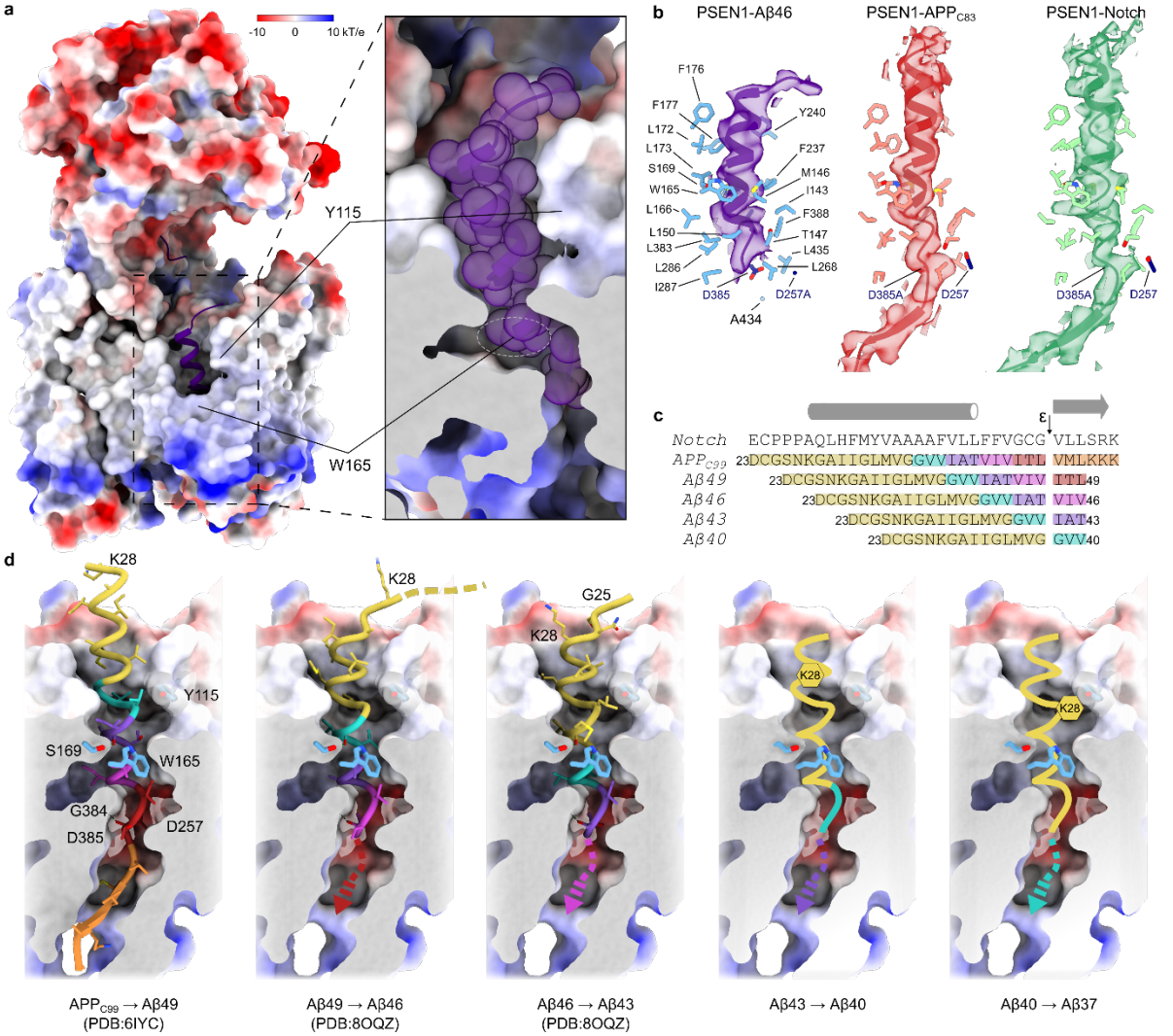


**Figure 6. Substrate interaction with GSEC and the model of sequential catalysis. a**, Surface representation of GSEC coloured by electrostatic potential and Aβ46 shown as cartoon. Fenestration in the intracellular membrane leaflet region of PSEN1 partially exposes Aβ46 to the membrane environment. **b,** Structure of substrate-binding channel of PSEN1 is identical with three different substrates and the conformations of the three substrates are very similar. **c,** Sequence alignment of Notch and the $APP_{C99}$ downstream products along the Aβ49 pathway. The initial endopeptidase cleavage site is indicated with the arrow and different colours indicate the tripeptides sequentially cleaved in the Aβ40 product line. **d,** A model of sequential catalysis. The structures of substrates in positions corresponding to the cuts producing known Aβ peptides are shown. Panels 1 and 3 counted from the left side are experimental structures, the remaining panels are models.

The GSEC-Aβ46 structure also showed that a hydrogen bond between a carbonyl oxygen in the C-terminally extended backbone of the substrate and the backbone nitrogen of Gly384$^{PSEN1}$ is preserved in both initial and intermediate substrates (**Figure 5d**). The latter is part of the conserved active site GX**G**D motif of aspartyl intramembrane proteases[36] (**Figure 5d**). The AD-linked Gly384A$^{PSEN1}$ [37,38] destabilises GSEC-Aβ interactions[18], supporting a stabilising role of the hydrogen-bonding interaction between Gly384$^{PSEN1}$ and the substrate's backbone.

On the cytoplasmic side, the density of Aβ46 ends with a two-residue stretch in an unwound conformation next to the catalytic Asp385$^{PSEN1}$ (**Figures 2 and 5**). In contrast, the initial endopeptidase substrates[20,21] have a 6-residue-long ordered extension in a β-strand conformation (**Figure 6b**) that forms the hybrid β-sheet, contributed by PSEN1 TM6-TM7 loop (residues 287-289 and 379-381) on one side and TM8-TM9 loop (residues 430-432) on the other (**Figure 5c**). In the GSEC1B-Aβ46 model, the PSEN1 TM8-TM9 loop is shifted away by 3.4 Å from the remaining two β-strands (**Figure 5c**).

Collectively, these data show that the substrate conformation is similar between initial and intermediate cuts, suggesting that GSEC shapes the substrate as the substrate rearranges during processive proteolysis at its C-terminus. In addition, the E-S bonding is stabilised by several polar interactions which likely also facilitate the unwinding of the substrate α-helix in the membrane.

## Discussion

Close to 300 mutations in GSEC cause early-onset familial AD. These pathogenic mutations destabilise the interaction between GSEC and APP, thus enhancing the release of longer and more hydrophobic Aβ peptides. Molecular understanding of the mechanisms underlying the modulation of the Aβ length will facilitate the development of drugs safely and efficiently targeting GSEC in AD therapy. To gain insights into the mechanisms modulating and defining Aβ length, we determined high-resolution structures of GSEC complexes containing the APH-1B isoform in apo state and bound to Aβ46, then we interrogated GSEC-Aβ interactions to identify the key determinants of E-S stability.

APH-1 serves as an essential scaffold during the assembly of the GSEC complex[39,40] and modulates its proteolytic activity in an isoform-dependent manner[11], APH-1A type GSECs generate shorter Aβ products, relative to the APH-1B type GSECs. Comparison of GSEC1B and the reported GSEC1A[20,28] structures revealed that differences in APH-1 are confined to regions with low sequence conservation between the isoforms (**Figure 3e**). These differences are consistent between the apo (**Figure 3)** and substrate-bound GSEC structures (**Supplementary Figure 5a**), regardless of the used lipid-mimetic environments (lipid nanodiscs, amphipols and digitonin). These findings suggest that the structural differences in APH-1 are sequence- rather than environment-dependent, which is further corroborated by the APH-1 structures predicted by AlphaFold2 (**Supplementary Figure 5b**).

Structurally variable regions in APH-1 isoforms (**Figure 3e**) map to the interface with PSEN1. Particularly interesting is the TM3-TM4$^{APH-1}$ loop which changes conformation upon substrate binding and moves concertedly with cytosolic end of TM1$^{PSEN1}$ and TM8$^{PSEN1}$ (**Figure 4b**). These TMs in PSEN1 play a key role in substrate cleavage[30,32,33]. Even though the conformation of TM1$^{PSEN1}$ is identical between substrate-bound GSEC1A and GSEC1B, the APH-1 isoforms may alter the dynamics of this structural triad (TM3-TM4$^{APH-1}$ loop, TM1$^{PSEN1}$ and TM8$^{PSEN1}$), thereby changing enzyme processivity. This proposal is supported by the effect of AD-linked P88L mutation in TM1$^{PSEN1}$ [34], which replaces the helix-breaking Pro with a

helix-forming Leu. This aggressive pathogenic PSEN1 variant exerts marked destabilising effects on GSEC-Aβ interactions[18] and thereby promotes the release of partially digested Aβ peptides, including very long Aβ45/46 peptides *in vitro*[33]. Similar to this pathogenic mutation, differences in the environment surrounding $TM1^{PSEN1}$ provided by APH-1A or APH-1B isoforms may change its dynamics and, consequently, alter GSEC processivity.

The structure of substrate-binding channel within PSEN1, that includes the conformation of side chains and backbones of the residues lining the channel, is virtually identical in the different GSEC-substrate complexes with Aβ46, $APP_{C83}$[20] and Notch[21] (**Figure 6b**). This indicates that substrate recognition and associated conformational changes in PSEN1 and substrate are largely independent of the substrate sequence (**Figure 6c**) and length, and are defined by GSEC.

In contrast with $APP_{C83}$ and Notch structures[20,21], the conformation of the functionally important loop 1 is different in the GSEC-Aβ46 complex (**Figure 5b** and **Supplementary Figure 6**). The differences are likely caused by the engineered cysteine bridge used to stabilise $APP_{C83}$ and Notch substrates within GSEC1A (**Supplementary Figure 6a**). Accordingly, the conformations of loop1 in the inhibitor-bound and unmodified structures determined in the absence of added substrate[26–28] and in GSEC-Aβ46 complex are identical (**Supplementary Figure 6b**).

Similar to $APP_{C83}$ and Notch, the Aβ46 helix is partially unwound close to the scissile bond and stabilised by plausible hydrogen bonds between its backbone and PSEN1 sidechains Trp165, Ser169 and Gly384 (**Figure 5a, d**). Additionally, in the unperturbed conformation of loop 1, Tyr115 points in the direction of substrate suggesting an E-S polar interaction inside the membrane bilayer (**Figure 5b**). Because we have previously shown that GSEC-Aβ complex stability defines enzyme processivity and Aβ length[18], we investigated the contribution of the polar Tyr115, Trp165 and Ser169 residues to the processing of $APP_{C99}$ in cells (**Figure 5e, f**). Removal of polar groups by mutagenesis reduced processivity in all instances suggesting a significant stabilising effect of the E-S hydrogen bonds. Furthermore, for Tyr115 even stronger reduction of processivity was observed after removal of the aromatic ring pointing towards contribution of Van der Waals interactions to the stabilisation of E-S interactions.

These data explain the pathogenic increases in longer Aβs by FAD mutations targeting these positions (Y115H, Y115C[41,42], W165C, S169P, S169L, ΔS169[43–46]). Moreover, our previous studies have shown that the FAD-linked G384A mutation generates longer Aβ peptides[18]. All of these mutations eliminate the hydrogen-bond-donating sidechains or change the location of the hydrogen-bond-donating atoms; thus suggesting that they reduce processivity by disturbing the hydrogen bonds stabilising the partially unwound Aβ α-helix.

In the structures of GSEC1A-$APP_{C99}$ or -Notch, the substrates downstream from the scissile bond had extended conformations and contributed a strand to a hybrid β-sheet [20,21] (**Figure 5c**). The latter is proposed to play important roles in stabilising substrate binding and orienting the scissile peptide bond towards the catalytic aspartates[21]. In GSEC1B-Aβ46 structure, the density of the substrate stops after the scissile bond, and the density of the hybrid β-strand – previously seen for endopeptidase substrates – is absent. This raises the following scenarios: the carboxypeptidase-like cleavages do not require the formation of the hybrid β-sheet, or the hybrid β-sheet is absent because the equilibrium of distribution of bound Aβ46 in the substrate-binding transmembrane channel is shifted towards Aβ46 bound as a product generated upon Aβ49 cleavage, rather than as a substrate for the Aβ46 → Aβ43 cut (**Figure 6a, d**). We believe that the first scenario is unlikely given that a formation of a β-sheet between substrate and protease is found in all studied proteases[47] and given a pattern of 3 to 4 amino acids cut steps.

It remains unclear how substrate rearranges its structures to deliver amino acids located 9 to 12 positions upstream from the first cut to the catalytic site (**Figure 6c**). The following models are suggested: (1) a piston model in which the transmembrane helical region of the substrate shifts into the hydrophobic region of PSEN1 channel, bringing polar substrate region inside the membrane; (2) a model according to which the transmembrane helical region gradually unwinds[21] or (3) both, progressive C-terminal unwinding of the transmembrane helical region with catalysis and partial substrate threading (piston movement)[18].

In GSEC1B-Aβ46 structure the extracellular part of the transmembrane helix of Aβ46 is embedded by ~ 4.5 Å (nearly one α-helical turn) deeper into the channel, relative to the initial $APP_{C83}$/Notch substrates. Our structure supports the piston model, at least during the first steps of the processive proteolysis, schematically shown in **Figure 6d.**

As a consequence of the Aβ α-helix embedding into the substrate channel, positively charged Lys28 must move inside the hydrophobic substrate channel for the Aβ40 → Aβ37 cut (**Figure 6d**). Even though this process might be facilitated by Tyr115, embedding a charged residue into a hydrophobic environment is energetically costly. Consistently, the fraction of released Aβ37 is low as compared to Aβ40[48]. This mechanism is also supported by our recent data demonstrating that charged/polar residues in the ectodomain of the APP limit substrate threading and promote product release[49].

In conclusion, our structural and functional analyses provide insights into the allosteric-like modulation of GSEC by the APH-1 isoforms, define the interaction of Aβ46 with GSEC and the contribution of polar E-S interactions including newly identified Tyr115 in loop 1. The described structures and functional data deliver novel structural frameworks in a native-like environment for fundamental and translational research into the mechanisms underlying GSEC-mediated proteolysis and discovery of drugs that can safely and efficiently tackle toxic Aβ production.

## Data Availability

The newly generated cryo-EM density maps and refined atomic models have been deposited to the PDB and EMDB databases under accession codes: 8OQY and EMD-17112 for the GSEC1B apo structure, and 8OQZ and EMD-17113 for the GSEC1B-Aβ46 structure.

**Acknowledgments** We thank Annelore Stroobants for technical support, Dr. Marcus Fislage and Dr. Adam Schröfel for assistance with cryo-EM data collection. We would like to acknowledge the funding provided by the VIB international PhD program fellowship to I.O. and Fonds Wetenschappelijk Onderzoek (Grant Nos. G0H5916N, G054617N to R.G.E. and G0B2519N, G008023N to L.C.G).

## Author Contributions

I.O. purified GSEC, reconstituted it into lipid nanodiscs, prepared cryo-EM grids, collected cryo-EM data, determined and analysed cryo-EM structures, analysed data, prepared figures, and wrote the original draft of the manuscript. M.B.S. performed the activity assays. S.L. performed cloning and generated the baculoviruses. L.C.G. and R.G.E. conceived, managed, and supervised the project, analysed data, reviewed, and edited the manuscript. I.O., L.C.G. and R.G.E. acquired funding.

**Competing interest statement** Authors declare no competing interests.

# Materials and methods

## GSEC1B expression, purification and formation of GSEC1B-Ab46 complex

Human NCT, PSEN1, APH-1B and PEN-2 were expressed in High Five insect cells using a baculovirus expression system as previously described[11]. NCT was cloned with a PreScission protease cleaving site and GFP tag at the C-terminus. The same system was used to express inactive GSEC1B complex (GSEC1B$^{D257A}$) in which PSEN1 was expressed as N- and C-terminal fragments (amino acids 1-297 and 298-467, respectively) to mimic the autoproteolytic activation of GSEC.

All the purification steps were carried out at 4°C. 72 hours after infection, cells were collected by centrifugation (4,800 x g, 20 min) and resuspended in 100 ml per litre of culture of lysis buffer (25 mM PIPES pH 7.4, 300 mM NaCl, 10% glycerol, 1x Complete protease inhibitor cocktail (Roche)). Resuspended cells were lysed using Emulsiflex C3 homogeniser (Avestin) and total membrane fractions isolated by ultracentrifugation (100,000 x g, 1 h). Membrane pellets were washed twice in 50 ml per litre of culture membrane in high-salt wash buffer (25 mM PIPES pH 7.4, 1 M NaCl, 10% glycerol); pellets were resuspended using a PTFE plunger in a Heidolph overhead stirrer, incubated on a rotator for 30 minutes and pelleted by ultracentrifugation. Washed membranes were resuspended in solubilisation buffer (25 mM PIPES, 300 mM NaCl, 2% CHAPSO (Anatrace), 5% glycerol, 1 x Complete protease inhibitor cocktail). After overnight incubation at 4°C, the soluble fraction was separated by ultracentrifugation and incubated overnight with agarose resin NHS-coupled to anti-GFP nanobodies[50] (NHS-activated Sepharose 4 FF; Cytiva). Resin was transferred into a gravity column (Bio-Rad) and washed with 20 column volumes (CV) of solubilisation buffer followed by 10 CV of wash buffer (25 mM PIPES, 300 mM NaCl, 1% CHAPSO, 0.1% 1-palmitoyl-2-oleoyl-glycero-3-phosphocholine (POPC; Avanti), 5% glycerol) and 10 CV of elution buffer (25 mM PIPES, 150 mM NaCl, 1% CHAPSO, 0.1% POPC, 1 mM dithiothreitol (DTT), 1 mM ethylenediaminetetraacetic acid (EDTA)). Next, the resin was resuspended in 1 CV of elution buffer and GSEC1B was eluted by overnight incubation with 50 µg/ml of PreScission protease[51]. To remove PreScission protease, the eluted faction was incubated overnight with Glutathione Sepharose 4B resin (Cytiva). Protein concentration was estimated using Bradford reagent (Bio-Rad) following the manufacturer's instructions and was in the 0.7-1.5 mg/ml range. Protein purity was assessed with SDS-PAGE (4-12% Bis-Tris; Invitrogen) and Coomassie staining (InstantBlue; Abcam). Purified protein was flash-frozen and stored at -80°C.

To form GSEC1B-Aβ46 complex, 5 µM Aβ46 (rPeptide) resuspended in dimethyl sulfoxide (DMSO) was added to purified GSEC1B$^{D257A}$ (1.25 x fold excess), followed by a 1 h incubation at 37°C.

## Expression and purification of membrane scaffold protein

Plasmid with MSP1D1, pMSP1D1[52] (Addgene) was transformed into *E. coli* BL21(DE3) competent cells. Culture was grown in LB medium containing 25 µg/ml kanamycin at 37°C until $OD_{600}$ of 0.8. Protein expression was induced by adding 1 mM IPTG and carried out for 3 h. Cells were collected by centrifugation (4,800 x g, 20 min, 4°C) and the pellet stored at -20°C.

All the purification steps were carried out at 4°C. Cell pellet was resuspended in 50 ml per litre of culture lysis buffer (150 mM Tris pH 8, 300 mM NaCl, 20 mM imidazole pH 8, 2.5 mM $MgCl_2$, 0.1 mM $CaCl_2$) and incubated with a few grains of DNAse I (Sigma) for 1 h. Resuspended cells were lysed using a continuous flow cell disruptor (Constant Systems) and

supplemented with 1% Triton X-100. Cell lysate was centrifuged (40,000 x g, 20 min), and the supernatant was filtered through a 0.45 µm filter before it was applied onto a HisTrap HP (Cytiva) column using an ÄKTA pure system (Cytiva). The column was washed with 10 CV of wash buffer 1 (40 mM Tris pH 8, 300 mM NaCl, 20 mM imidazole pH 8, 1% Triton X-100); 10 CV of wash buffer 2 (40 mM Tris pH 8, 300 mM NaCl, 20 mM imidazole pH 8, 2.15% sodium cholate (Sigma), 1% Triton X-100); 10 CV of wash buffer 3 (40 mM Tris pH 8, 300 mM NaCl, 20 mM imidazole pH 8, 1% sodium cholate); and 10 CV of wash buffer 4 (40 mM Tris pH 8, 300 mM NaCl, 50 mM imidazole pH 8, 1% sodium cholate). MSP1D1 was eluted using a gradient of imidazole (from 50 to 400 mM) over 10 CV in wash buffer 4. The peak fractions containing MSP1D1 were pooled and dialysed overnight in 3.5 kDa MWCO cellulose tubing (Carl Roth) against 80 x volume of dialysis buffer (40 mM Tris pH 8, 150 mM NaCl) to remove excess imidazole. Protein concentration was measured spectrophotometrically ($\varepsilon_{280}$ 21430 $M^{-1}cm^{-1}$, MW 24.79 kDa) using NanoDrop One (Thermo Scientific). Dialysed MSP1D1 was concentrated to 5 mg/ml using a 10 kDa MWCO Amicon Ultra centrifugal concentrator (Millipore), supplemented with CHAPSO (4%) and DTT (2 mM) and, to cleave the His-tag, the sample was incubated overnight with TEV protease (1 µg of TEV protease per 100 µg of MSP). The TEV protease was expressed and purified as previously described[53]. Cleaved MSP1D1 was applied onto a HisTrap HP column (Cytiva), the flowthrough containing untagged MSP1D1 was collected, concentrated to 5 mg/ml, and further purified by size exclusion chromatography using a Superdex 75 column (Cytiva) in SEC buffer (25 mM PIPES pH 7.4, 150 mM NaCl, 0.5% CHAPSO). Protein concentration was measured spectrophotometrically ($\varepsilon_{280}$ 18450 $M^{-1}cm^{-1}$, MW 22.04 kDa). Fractions containing pure untagged MSP1D1 were pooled and concentrated to ~10 mg/ml, then flash frozen and stored at -80°C.

## Reconstitution of GSEC1B in lipid nanodiscs

We screened reconstitution conditions including two constructs of membrane scaffold protein (MSP) and two lipid compositions. The optimal reconstitution was obtained using MSP1D1 and POPC:DLPC (1,2-dilauroyl-sn-glycero-3-phosphocholine; Avanti) mix at 1:1 molar ratio.

All the steps were carried out at 4°C. Purified GSEC1B or GSEC1B-Aβ46 complex at a concentration of 0.7-1.5 mg/ml was diluted with a solution containing 10% CHAPSO and 1.67% 1,2-dilauroyl-sn-glycero-3-phosphocholine (DLPC; Avanti) to a final concentration of 1.2 mM POPC and 2.4 mM DLPC and the solution was stirred for 30 min. MSP1D1 was added to the solution to obtain the MSP:POPC:DLPC molar ratio of 1:60:80 and the solution was stirred for 1 h. Reconstitution of nanodiscs was achieved upon detergent adsorption by Bio-Beads SM-2 resin (Bio-Rad) which was added in three batches, 0.25 g/ml each, and the protein solution was incubated while stirring for 1 h after the first batch, overnight after the second, and 1 h after the third. Nanodiscs were collected from the tube by centrifugation after puncturing the bottom of the tube. The reconstituted GSEC1B in nanodiscs was separated from empty nanodiscs by size exclusion chromatography using a Superdex 200 Increase column (Cytiva) in SEC buffer (10 mM PIPES pH 7.4, 100 mM NaCl). SDS-PAGE and silver staining (Pierce silver stain kit; Thermo Scientific) were used to assess the contents of the fractions.

Peak fractions containing GSEC1B were concentrated to 0.04-0.1 mg/ml using a 100 kDa MWCO Amicon Ultra centrifuge filter (Millipore).

## GSEC1B activity assays

The activity assays were carried out at 37°C in a Labcycler Gradient thermocycler (SensoQuest). Final buffer composition of the reactions was 25 mM PIPES, 150 mM NaCl, 0.025% DMSO. Assays were carried out with 0.24 µM GSEC1B and 2.5 µM Aβ46 for 4 h.

Reactions were quenched by placing the assay tubes on ice and adding 10 μM inhibitor L-685,458 (Santa Cruz Biotechnology). De novo Aβ40 production was quantified by MSD ELISA as described previously[48]. The plots were generated using GraphPad Prism version 8.4.2.

## Generation of MEF cell lines and the cell-based activity assays

Single-point mutations (Y115A, Y115F, W165F and S169A) were introduced into human PSEN1 cDNA cloned into the pMSCVpuro vector using Q5 Site-Directed Mutagenesis Kit (NEB BioLabs) according to the standard protocol. To generate recombinant retroviruses, the generated vectors and the PIK packaging plasmid were delivered into HEK 293T cells using the TransIT-LT1 transfection reagent (Mirus Bio). Stable MEF cell lines expressing either wild-type (WT) or mutant PSEN1/GSEC complexes were generated through retroviral transduction of *Psen1*$^{-/-}$/*Psen2*$^{-/-}$ mouse embryonic fibroblasts (MEFs)[54] as previously described[48]. MEFs were cultured in Dulbecco's Modified Eagle's Medium (DMEM)/F-12 (Life Technologies) supplemented with 10% fetal bovine serum (FBS) (Sigma-Aldrich)[35]. Cell lines stably expressing the WT/mutant proteins were selected using media supplemented with 5 μg/ml puromycin (Sigma-Aldrich). The reconstitution of mutant GSECs was assessed by SDS-PAGE/western blotting. Briefly, cells were collected, and total membranes isolated and solubilised in 28 mM PIPES pH 7.4, 210 mM NaCl, 280 mM sucrose, 1.5 mM EGTA pH 8, 1% CHAPSO, 1x Complete protease inhibitor cocktail. Equal amounts of solubilised protein were resolved in a 4–12% Bis-Tris NuPAGE gel (ThermoScientific) and transferred to a nitrocellulose membrane. The membrane was blotted with the following antibodies: anti-human PSEN1-CTF (MAB5643; Merck Millipore); anti-PEN2 (D6G8; Cell signalling) and anti-NCSTN (9C3; kindly provided by Prof. Wim Annaert). We used the following secondary antibodies: horseradish peroxidase-conjugated anti-mouse (#1721011, Bio-Rad) or anti-rabbit IgG (#1721019 Bio-Rad). Blots were developed using Western Lightning Plus-ECL Enhanced Chemiluminescence Substrate (Perkin Elmer).

To assess the effects of PSEN1 mutants on Aβ production, $APP_{C99}$ substrate was transiently expressed in the generated MEF cell lines using a recombinant adenoviral expression system as previously described[55]. In brief, cells were plated in a 96-well plate at the density of 12,500 cells/well and transduced 6-8 h later with Ad5/CMV-$APP_{C99}$ adenovirus[48]. The culture medium was replaced with a low-serum medium (DMEM/F-12 medium containing 0.2% FBS) 16 h later, and collected after a 24 h incubation period at 37°C.

The conditioned media was cleared by centrifugation at 800 x g for 15 min and used to determine Aβ37, Aβ38, Aβ40 and Aβ42 peptide levels using multiplex Meso Scale Discovery (MSD) ELISA, as previously described. Briefly, 96-well MSD ELISA plates precoated with anti-Aβ37, Aβ38, Aβ40, and Aβ42 antibodies were blocked in phosphate buffer saline (PBS) supplemented with 0.1% casein. Freshly harvested conditioned medium or Aβ standards (recombinant human Aβ1-37, Aβ1-38, Aβ1-40, and Aβ1-42 peptides at known concentrations; rPeptide) were mixed (1:1 V/V) with SULFO-TAG–conjugated 6E10 detection antibody (diluted in blocking buffer) and loaded on the plate (50 μl sample/well). Following overnight incubation at 4°C, ELISA plates were rinsed five times with washing buffer (PBS supplemented with 0.05% Tween 20) and immediately measured in MSD Gold read buffer (MSD) (150 μl/well) on a Sector Imager 6000 (MSD). Statistical analysis was performed using GraphPad Prism version 8.4.2.

## Preparation of graphene oxide coated EM grids

Carbon-coated holey grids Quantifoil R 0.6/1 Cu 300 and CF-2/1-3C (EMS) were used for preparing cryo-EM samples for apo GSEC1B and GSEC1B-Aβ46 complex, respectively. Graphene oxide 0.2% (w/v; Sigma) and 1% (w/v; GOgraphene) were used interchangeably.

Grids were glow-discharged with carbon face up using ELMO glow discharge system (Agar Scientific) with 5 mA current for 1 min at 0.3 mbar in air. A volume of 4 µl of 0.5 mg/ml poly-L-lysine solution (MW 15-30 kDa; Sigma) in 10 mM PIPES pH 7.4, 100 mM NaCl was pipetted on the carbon side of the grid and incubated for 2 min, blotted with Whatman grade 2 paper and washed twice by pipetting 4 µl of MilliQ water on the carbon side, followed by blotting. After 5 min drying on air, 3 µl of 0.2 mg/ml graphene oxide was pipetted on carbon side of the grid and incubated for 2 min. Next, the grid was blotted, and washed three times by touching a droplet of water with the GO side, followed by blotting. The grid was dried for 30 min and 4 µl of 0.1% PEG 10,000 (Fluka Chemica) in 10 mM PIPES pH 7.4, 100 mM NaCl was applied on the carbon side of the grid and incubated for 2 min. The grid was blotted and washed twice by pipetting 4 µl of water on top and blotting. The grid was dried for 5 min and used for preparation of cryo-EM samples immediately.

## Cryo-EM sample preparation

GSEC1B nanodisc solution (2 µl) at concentration of 0.04 mg/ml was pipetted on the front side of graphene-oxide-coated ('MRC protocol'[56]) Quantifoil R 0.6/1 Cu300 grid and incubated for 15-30 sec at 99% humidity in a Cryoplunge 3 (Gatan). The grid was blotted from both sides for 2.5-3 sec with Whatman grade 3 paper and plunged into liquid ethane at -175°C.

For the GSEC1B-Aβ46 complex, 5 µM Aβ46 (15-fold excess) resuspended in DMSO was added to GSEC1B-Aβ46 reconstituted into lipid nanodiscs (1% final DMSO concentration) and the mix was incubated for 1 h at 37°C. Next, the protein solution was cooled on ice and plunge frozen on CF-2/1-3C grids coated with graphene oxide (according to the protocol described in the section above) as described for the apo protein complex.

## Cryo-EM data collection

The micrographs were collected on a CRYO ARM 300 electron cryogenic microscope (JEOL) equipped with an in-column Omega energy filter and operated at 300 keV. The energy filter slit was set to 20 eV and the data were collected at a nominal magnification of 60,000 with a magnified pixel size of 0.766 Å on a K3 direct electron detector (Gatan). SerialEM (3.8.2 for apo, 3.8.18 for Aβ46-bound data) was used for automated data collection.

The micrographs for GSEC1B in apo state were collected as 60-frame movies with an electron dose of 1.06 $e^{-}$ $Å^{-2}$ per frame over 3 seconds in a 5x5 pattern with one exposure per 0.6 µm nominal and 0.3 µm measured hole diameter, producing 25 micrographs per stage position. A total of 10,733 movies were collected from one EM grid with the defocus in the range from -1.2 to -2 µm.

For the GSEC1B-Aβ46 complex the micrographs were collected in a 3x3 pattern with 5 exposures per each 2 µm hole resulting in 45 movies per stage position. Each movie contained 60 frames with total exposure of 2.8 s and an electron dose of 0.936 e- $Å^{-2}$ per frame. A total of 18,855 movies were collected. The defocus was set to -1.3 to -2.3 µm.

## Image processing

Movies were pre-processed on-the-fly using RELION 3.1 schedules[57] as a wrapper to run MotionCor2 1.4.2[58] for frame alignment and CTF parameters were estimated using CTFFIND 4.1.14[59]. Further processing was done using RELION 3.1 unless otherwise stated. Particles

from a subset of micrographs were auto-picked using crYOLO 1.7[60] with the general model and submitted to 2D classification in either RELION or cryoSPARC (v3.2.0 for the apo dataset, v3.3.1 for the Aβ46-bound dataset)[61]. 100 micrographs containing the highest number of particles from good classes were manually screened to remove bad particles, then these micrographs and particle coordinates were used to refine the crYOLO general picking model. The refined model was used to auto-pick the entire dataset.

For the apo dataset, 986,830 particles were picked from 5501 micrographs and extracted in a 320x320 pixel box downsampled to 64x64 pixels (**Extended Data Figure 2**). 2D classification was done in RELION (ignoring CTFs until the first peak) and in cryoSPARC (setting initial classification uncertainty factor to 20, online-EM iterations to 100, final full iterations to 20, batch size per class to 1000, enforcing non-negativity, activating clamp-solvent option, disabling FRC-based regularizer, full FRC, setting iteration to start annealing sigma to 10, number of iterations to anneal sigma to 50, and using white noise model). Particles belonging to good 2D classes from both programs were merged and duplicate particles removed resulting in a total of 790,832 particles which were then reextracted in a 320x320 pixel box downscaled to 128x128 pixels. Ab-initio reconstruction in cryoSPARC was used to generate an initial model from a subset of particles. 3D classification with 1 class and using tau_fudge value of 64 was used to centre and align the particles. 3D classification with 4 classes and tau_fudge value of 64 resulted in 2 classes with visible transmembrane helices accounting for 413,321 particles which were then reextracted in a 320x320 pixel box downscaled to 256x256 pixels. 3D auto-refinement of these particles resulted in a map resolved to an average resolution of 3.8 Å. Next, 3D classification without alignment with 2 classes and tau_fudge value of 8 was used to separate particles contributing to high-resolution reconstruction and resulted in 115,197 particles. A 3.6 Å map was reconstructed from these particles which was improved to 3.3 Å after reextracting in a 320x320 pixel box without downsampling, Bayesian polishing and defocus refinement. To better resolve the transmembrane region, another round of 3D refinement was performed using external reconstruction with SIDESPLITTER[62] which resulted in the final map at a resolution of 3.2 Å. The final map was sharpened using post process procedure in RELION. The pixel size was calibrated using the NCT ectodomain from the GSEC1A-C83 structure (PDB: 6IYC) as a reference in UCSF Chimera[63], by fitting the reference model into the experimental map. The final map was rescaled and sharpened using the calibrated pixel size of 0.776 Å yielding a 3.3 Å map. The map was further filtered using local resolution filter and the B-factor determined during post processing. The local filtered map was used for model building and deposited.

For the GSEC1B-Aβ46 complex, 2,788,683 particles were picked from 18,855 micrographs and classified in 2D as described above (**Extended Data Figure 4**). 2,433,778 particles selected after 2D classification were centred and aligned using a 3D classification with 1 class and using tau_fudge value of 64. 3D classification with 10 classes, tau_fudge value 64 over 75 iterations was done using a low-pass filtered map from the apo dataset as a reference model. 3D classes with visible transmembrane helices from iterations 51-75 were picked and duplicate particles removed for a total of 2,023,687 particles which were then subjected to 3D refinement to obtain a map resolved to 4.1 Å. The densities for PSEN1 TM2 and Aβ46 were very weak. Further 3D classification of these particles (K=10; T=4; 3.7° sampling; 15° search range; 25 iterations) resulted in two high-resolution classes containing 397,175 particles which were subjected to 3D refinement and resulted in a 3.5 Å map with improved, but still weak densities of PSEN1 TM2 and Aβ46. CTF refinement including anisotropic magnification, beam tilt, trefoil, per particle defocus and per micrograph astigmatism followed by Bayesian polishing improved the resolution of the reconstruction to 3.3 Å. A mask containing PSEN1 and Aβ46 density was used to subtract the rest of the signal and the subtracted particles were subjected

to 3D classification without alignment (K=10; T=32; 400 iterations) which resulted in a class containing 53,612 particles with improved densities of PSEN1 TM2 and Aβ46. These particles were reverted and subjected to 3D refinement which yielded a map resolved to 3.4 Å. The pixel size was calibrated to 0.949 (320x320 pixel box downscaled to 256 pixels) and the map was postprocessed, sharpened and filtered in the same way as described above, yielding a 3.4 Å map. The local filtered map was used for model building and deposited.

## Model building and refinement

For the apo structure, the starting model was obtained from the structure of GSEC1A in amphipols (PDB: 5FN5)[28] and rigid-body-fitted into the EM density using UCSF Chimera[63]. A model of APH-1B was built with by homology modelling using modeller 9[64]. The model was further manually built and refined using Coot 0.9.8[65] after which it was refined using real-space refinement with simulated annealing in PHENIX 1.19.2[66]. Several iterations of manual rebuilding in Coot and automated refinement in PHENIX with secondary structure restraints were used to refine the model. The model was validated using MolProbity[67].

For the GSEC1B-Aβ46 structure, the starting model was obtained from the structure of GSEC1A-C83 (PDB: 6IYC)[20] from which the sugars, substrate and lipids were removed. Aβ46 was manually built as a poly alanine model. PSEN1 loop 1 (amino acids 106-123) was manually built to fit into the density and the resulting PSEN1 model was used for template-based structure prediction using ColabFold[68,69] to aid manual building of loop 1. Further refinement and validation were done as described above.

To make structural comparison possible, the pixel size of the apo GSEC1A structure (EMDB-3240)[28] was calibrated and the map was rescaled in the same way as described above. To avoid reinterpreting the map, the model (PDB: 5FN5) was refined into the rescaled map using real-space refinement in PHENIX and the original model was fitted onto the backbone of the refined model five amino acids at a time with an overlap of two amino acids to keep the sidechain orientations intact.

Figures of atomic models and cryo-EM maps were generated using UCSF ChimeraX[70] version 1.4.

## Bioinformatics analysis

APH-1 sequences were aligned using Clustal Omega[71] and coloured using Jalview[72] version 2.11.2.6 according to BLOSUM62 score with a 40 % conservation threshold.

# References

1. Scheltens, P. *et al.* Alzheimer's disease. *Lancet* **397**, 1577–1590 (2021).
2. Matsumura, N. *et al.* γ-Secretase associated with lipid rafts: multiple interactive pathways in the stepwise processing of β-carboxyl-terminal fragment. *J Biol Chem* **289**, 5109–5121 (2014).
3. Takami, M. *et al.* gamma-Secretase: successive tripeptide and tetrapeptide release from the transmembrane domain of beta-carboxyl terminal fragment. *J Neurosci* **29**, 13042–13052 (2009).
4. Selkoe, D. J. & Hardy, J. The amyloid hypothesis of Alzheimer's disease at 25 years. *EMBO Molecular Medicine* **8**, 595–608 (2016).
5. Güner, G. & Lichtenthaler, S. F. The substrate repertoire of γ-secretase/presenilin. *Semin Cell Dev Biol* **105**, 27–42 (2020).

6. Jurisch-Yaksi, N., Sannerud, R. & Annaert, W. A fast growing spectrum of biological functions of γ-secretase in development and disease. *Biochimica et Biophysica Acta (BBA) - Biomembranes* **1828**, 2815–2827 (2013).
7. De Strooper, B., Iwatsubo, T. & Wolfe, M. S. Presenilins and γ-secretase: structure, function, and role in Alzheimer Disease. *Cold Spring Harb Perspect Med* **2**, (2012).
8. Sato, T. *et al.* Active -Secretase Complexes Contain Only One of Each Component. *Journal of Biological Chemistry* **282**, 33985–33993 (2007).
9. Lai, M.-T. *et al.* Presenilin-1 and presenilin-2 exhibit distinct yet overlapping gamma-secretase activities. *J Biol Chem* **278**, 22475–22481 (2003).
10. Shirotani, K., Edbauer, D., Prokop, S., Haass, C. & Steiner, H. Identification of distinct gamma-secretase complexes with different APH-1 variants. *J Biol Chem* **279**, 41340–41345 (2004).
11. Acx, H. *et al.* Signature Amyloid β Profiles Are Produced by Different γ-Secretase Complexes. *Journal of Biological Chemistry* **289**, 4346–4355 (2014).
12. Sannerud, R. *et al.* Restricted Location of PSEN2/γ-Secretase Determines Substrate Specificity and Generates an Intracellular Aβ Pool. *Cell* **166**, 193–208 (2016).
13. Serneels, L. *et al.* γ-Secretase Heterogeneity in the Aph1 Subunit: Relevance for Alzheimer's Disease. *Science* **324**, 639–642 (2009).
14. Schwartzentruber, J. *et al.* Genome-wide meta-analysis, fine-mapping and integrative prioritization implicate new Alzheimer's disease risk genes. *Nat Genet* **53**, 392–402 (2021).
15. Esch, F. S. *et al.* Cleavage of amyloid beta peptide during constitutive processing of its precursor. *Science* **248**, 1122–1124 (1990).
16. Vassar, R. *et al.* Beta-secretase cleavage of Alzheimer's amyloid precursor protein by the transmembrane aspartic protease BACE. *Science* **286**, 735–741 (1999).
17. Qi-Takahara, Y. Longer Forms of Amyloid Protein: Implications for the Mechanism of Intramembrane Cleavage by γ-Secretase. *Journal of Neuroscience* **25**, 436–445 (2005).
18. Szaruga, M. *et al.* Alzheimer's-Causing Mutations Shift Aβ Length by Destabilizing γ-Secretase-Aβn Interactions. *Cell* **170**, 443-456.e14 (2017).
19. Chávez-Gutiérrez, L. & Szaruga, M. Mechanisms of neurodegeneration - Insights from familial Alzheimer's disease. *Semin Cell Dev Biol* **105**, 75–85 (2020).
20. Zhou, R. *et al.* Recognition of the amyloid precursor protein by human γ-secretase. *Science* **363**, (2019).
21. Yang, G. *et al.* Structural basis of Notch recognition by human γ-secretase. *Nature* **565**, 192–197 (2019).
22. Autzen, H. E., Julius, D. & Cheng, Y. Membrane mimetic systems in CryoEM: keeping membrane proteins in their native environment. *Curr Opin Struct Biol* **58**, 259–268 (2019).
23. Glaeser, R. M. Proteins, interfaces, and cryo-EM grids. *Current Opinion in Colloid & Interface Science* **34**, 1–8 (2018).
24. Glaeser, R. M. & Han, B.-G. Opinion: hazards faced by macromolecules when confined to thin aqueous films. *Biophys Rep* **3**, 1–7 (2017).
25. Patel, A., Toso, D., Litvak, A. & Nogales, E. Efficient graphene oxide coating improves cryo-EM sample preparation and data collection from tilted grids. Preprint at https://doi.org/10.1101/2021.03.08.434344 (2021).
26. Guo, X. *et al.* Molecular basis for isoform-selective inhibition of presenilin-1 by MRK-560. *Nat Commun* **13**, 6299 (2022).
27. Yang, G. *et al.* Structural basis of γ-secretase inhibition and modulation by small molecule drugs. *Cell* **184**, 521-533.e14 (2021).
28. Bai, X., Rajendra, E., Yang, G., Shi, Y. & Scheres, S. H. Sampling the conformational space of the catalytic subunit of human γ-secretase. *eLife* **4**, 1–19 (2015).

29. Bai, X. *et al.* An atomic structure of human γ-secretase. *Nature* **525**, 212–217 (2015).
30. Wang, J., Brunkan, A. L., Hecimovic, S., Walker, E. & Goate, A. Conserved 'PAL' sequence in presenilins is essential for gamma-secretase activity, but not required for formation or stabilization of gamma-secretase complexes. *Neurobiol Dis* **15**, 654–666 (2004).
31. Takagi-Niidome, S., Osawa, S., Tomita, T. & Iwatsubo, T. Inhibition of γ-secretase activity by a monoclonal antibody against the extracellular hydrophilic loop of presenilin 1. *Biochemistry* **52**, 61–69 (2013).
32. Cai, T., Yonaga, M. & Tomita, T. Activation of γ-Secretase Trimming Activity by Topological Changes of Transmembrane Domain 1 of Presenilin 1. *J Neurosci* **37**, 12272–12280 (2017).
33. Ohki, Y. *et al.* Binding of longer Aβ to transmembrane domain 1 of presenilin 1 impacts on Aβ42 generation. *Mol Neurodegener* **9**, 7 (2014).
34. Liu, C. Y. *et al.* Two Novel Mutations in the First Transmembrane Domain of Presenilin1 Cause Young-Onset Alzheimer's Disease. *J Alzheimers Dis* **58**, 1035–1041 (2017).
35. Chávez-Gutiérrez, L. *et al.* The mechanism of γ-Secretase dysfunction in familial Alzheimer disease. *The EMBO Journal* **31**, 2261–2274 (2012).
36. Steiner, H. *et al.* Glycine 384 is required for presenilin-1 function and is conserved in bacterial polytopic aspartyl proteases. *Nat Cell Biol* **2**, 848–851 (2000).
37. Cruts, M. *et al.* Molecular genetic analysis of familial early-onset Alzheimer's disease linked to chromosome 14q24.3. *Hum Mol Genet* **4**, 2363–2371 (1995).
38. Tanahashi, H. *et al.* Sequence analysis of presenilin-1 gene mutation in Japanese Alzheimer's disease patients. *Neurosci Lett* **218**, 139–141 (1996).
39. LaVoie, M. J. *et al.* Assembly of the gamma-secretase complex involves early formation of an intermediate subcomplex of Aph-1 and nicastrin. *J Biol Chem* **278**, 37213–37222 (2003).
40. Niimura, M. *et al.* Aph-1 contributes to the stabilization and trafficking of the gamma-secretase complex through mechanisms involving intermolecular and intramolecular interactions. *J Biol Chem* **280**, 12967–12975 (2005).
41. Campion, D. *et al.* Mutations of the presenilin I gene in families with early-onset Alzheimer's disease. *Hum Mol Genet* **4**, 2373–2377 (1995).
42. Cruts, M. *et al.* Estimation of the genetic contribution of presenilin-1 and -2 mutations in a population-based study of presenile Alzheimer disease. *Hum Mol Genet* **7**, 43–51 (1998).
43. Campion, D. *et al.* Early-Onset Autosomal Dominant Alzheimer Disease: Prevalence, Genetic Heterogeneity, and Mutation Spectrum. *The American Journal of Human Genetics* **65**, 664–670 (1999).
44. Ezquerra, M. *et al.* A presenilin 1 mutation (Ser169Pro) associated with early-onset AD and myoclonic seizures. *Neurology* **52**, 566–570 (1999).
45. Taddei, K. *et al.* Two novel presenilin-1 mutations (Ser169Leu and Pro436Gln) associated with very early onset Alzheimer's disease. *Neuroreport* **9**, 3335–3339 (1998).
46. Guo, J. *et al.* A novel presenilin 1 mutation (Ser169del) in a Chinese family with early-onset Alzheimer's disease. *Neurosci Lett* **468**, 34–37 (2010).
47. Madala, P. K., Tyndall, J. D. A., Nall, T. & Fairlie, D. P. Update 1 of: Proteases universally recognize beta strands in their active sites. *Chem Rev* **110**, PR1-31 (2010).
48. Petit, D. *et al.* Extracellular interface between APP and Nicastrin regulates Aβ length and response to γ-secretase modulators. *The EMBO journal* **38**, (2019).
49. Koch, M. *et al.* APP ectodomain defines Aβ length by restraining γ-secretase processivity and facilitating product release. *The EMBO Journal* (In revision).
50. Rothbauer, U. *et al.* A versatile nanotrap for biochemical and functional studies with fluorescent fusion proteins. *Mol Cell Proteomics* **7**, 282–289 (2008).

51. Walker, P. A. *et al.* Efficient and rapid affinity purification of proteins using recombinant fusion proteases. *Biotechnology (N Y)* **12**, 601–605 (1994).
52. Denisov, I. G., Grinkova, Y. V., Lazarides, A. A. & Sligar, S. G. Directed self-assembly of monodisperse phospholipid bilayer Nanodiscs with controlled size. *J Am Chem Soc* **126**, 3477–3487 (2004).
53. Raran-Kurussi, S., Cherry, S., Zhang, D. & Waugh, D. S. Removal of Affinity Tags with TEV Protease. *Methods Mol Biol* **1586**, 221–230 (2017).
54. Herreman, A. *et al.* Total inactivation of gamma-secretase activity in presenilin-deficient embryonic stem cells. *Nat Cell Biol* **2**, 461–462 (2000).
55. Petit, D. *et al.* Aβ profiles generated by Alzheimer's disease causing PSEN1 variants determine the pathogenicity of the mutation and predict age at disease onset. *Mol Psychiatry* **27**, 2821–2832 (2022).
56. Bokori-Brown, M. *et al.* Cryo-EM structure of lysenin pore elucidates membrane insertion by an aerolysin family protein. *Nat Commun* **7**, 11293 (2016).
57. Scheres, S. H. W. W. RELION: Implementation of a Bayesian approach to cryo-EM structure determination. *Journal of Structural Biology* **180**, 519–530 (2012).
58. Zheng, S. Q. *et al.* MotionCor2: anisotropic correction of beam-induced motion for improved cryo-electron microscopy. *Nature methods* **14**, 331–332 (2017).
59. Rohou, A. & Grigorieff, N. CTFFIND4: Fast and accurate defocus estimation from electron micrographs. *Journal of structural biology* **192**, 216–21 (2015).
60. Wagner, T. *et al.* SPHIRE-crYOLO is a fast and accurate fully automated particle picker for cryo-EM. *Communications Biology* **2**, 218 (2019).
61. Punjani, A., Rubinstein, J. L., Fleet, D. J. & Brubaker, M. A. cryoSPARC: algorithms for rapid unsupervised cryo-EM structure determination. *Nature Methods* **14**, 290–296 (2017).
62. Ramlaul, K., Palmer, C. M., Nakane, T. & Aylett, C. H. S. Mitigating local over-fitting during single particle reconstruction with SIDESPLITTER. *J Struct Biol* **211**, 107545 (2020).
63. Pettersen, E. F. *et al.* UCSF Chimera - A visualization system for exploratory research and analysis. *Journal of Computational Chemistry* **25**, 1605–1612 (2004).
64. Sali, A. & Blundell, T. L. Comparative protein modelling by satisfaction of spatial restraints. *Journal of molecular biology* **234**, 779–815 (1993).
65. Emsley, P., Lohkamp, B., Scott, W. G. & Cowtan, K. Features and development of Coot. *Acta Crystallogr D Biol Crystallogr* **66**, 486–501 (2010).
66. Liebschner, D. *et al.* Macromolecular structure determination using X-rays, neutrons and electrons: recent developments in Phenix. *Acta Crystallogr D Struct Biol* **75**, 861–877 (2019).
67. Chen, V. B. *et al.* MolProbity: all-atom structure validation for macromolecular crystallography. *Acta Crystallogr D Biol Crystallogr* **66**, 12–21 (2010).
68. Jumper, J. *et al.* Highly accurate protein structure prediction with AlphaFold. *Nature* **596**, 583–589 (2021).
69. Mirdita, M. *et al.* ColabFold: making protein folding accessible to all. *Nat Methods* **19**, 679–682 (2022).
70. Pettersen, E. F. *et al.* UCSF ChimeraX: Structure visualization for researchers, educators, and developers. *Protein Sci* **30**, 70–82 (2021).
71. Sievers, F. *et al.* Fast, scalable generation of high-quality protein multiple sequence alignments using Clustal Omega. *Mol Syst Biol* **7**, 539 (2011).
72. Waterhouse, A. M., Procter, J. B., Martin, D. M. A., Clamp, M. & Barton, G. J. Jalview Version 2--a multiple sequence alignment editor and analysis workbench. *Bioinformatics* **25**, 1189–1191 (2009).

73. Bai, X., Rajendra, E., Yang, G., Shi, Y. & Scheres, S. H. W. Sampling the conformational space of the catalytic subunit of human γ-secretase. *eLife* **4**, (2015).
74. Yang, G. *et al.* Structural basis of γ-secretase inhibition and modulation by small molecule drugs. *Cell* **184**, 521-533.e14 (2021).
75. Guo, X. *et al.* Molecular basis for isoform-selective inhibition of presenilin-1 by MRK-560. *Nature communications* **13**, 6299 (2022).

## Table 1. Cryo-EM data collection, refinement, and validation statistics

| | #1 GSEC1B apo (EMDB-17112) (PDB 8OQY) | #2 GSEC1B-Aβ46 complex (EMDB-17113) (PDB 8OYZ) |
|---|---|---|
| **Data collection and processing** | | |
| Magnification | 60,000 | 60,000 |
| Voltage (kV) | 300 | 300 |
| Electron exposure (e–/Å$^2$) | 63.6 | 56.2 |
| Defocus range (μm) | -0.5 to -3.5 | -0.5 to -3.0 |
| Pixel size (Å) | 0.776 | 0.759 |
| Symmetry imposed | C1 | C1 |
| Initial particle images (no.) | 986,830 | 2,433,778 |
| Final particle images (no.) | 115,197 | 53,612 |
| Map resolution (Å) | 3.3 | 3.4 |
| FSC threshold | 0.143 | 0.143 |
| Map resolution range (Å) | 3.2 to 5.5 | 3.3 to 5.0 |
| | | |
| **Refinement** | | |
| Initial model used (PDB code) | 5FN5 | 6IYC |
| Model resolution (Å) | 3.3 | 3.4 |
| FSC threshold | 0.5 | 0.5 |
| Map sharpening *B* factor (Å$^2$) | -95.8 | -80.4 |
| Model composition | | |
| Non-hydrogen atoms | 9810 | 11131 |
| Protein residues | 1224 | 1340 |
| Ligands | 20 | 28 |
| *B* factors (Å$^2$) | | |
| Protein | 55.10 | 49.00 |
| Ligand | 45.11 | 42.18 |
| R.m.s. deviations | | |
| Bond lengths (Å) | 0.005 | 0.004 |
| Bond angles (°) | 0.923 | 0.849 |
| Validation | | |
| MolProbity score | 1.55 | 1.63 |
| Clashscore | 4.44 | 6.40 |
| Poor rotamers (%) | 0.71 | 0.27 |
| Ramachandran plot | | |
| Favored (%) | 95.28 | 95.92 |
| Allowed (%) | 4.55 | 3.85 |
| Disallowed (%) | 0.17 | 0.23 |

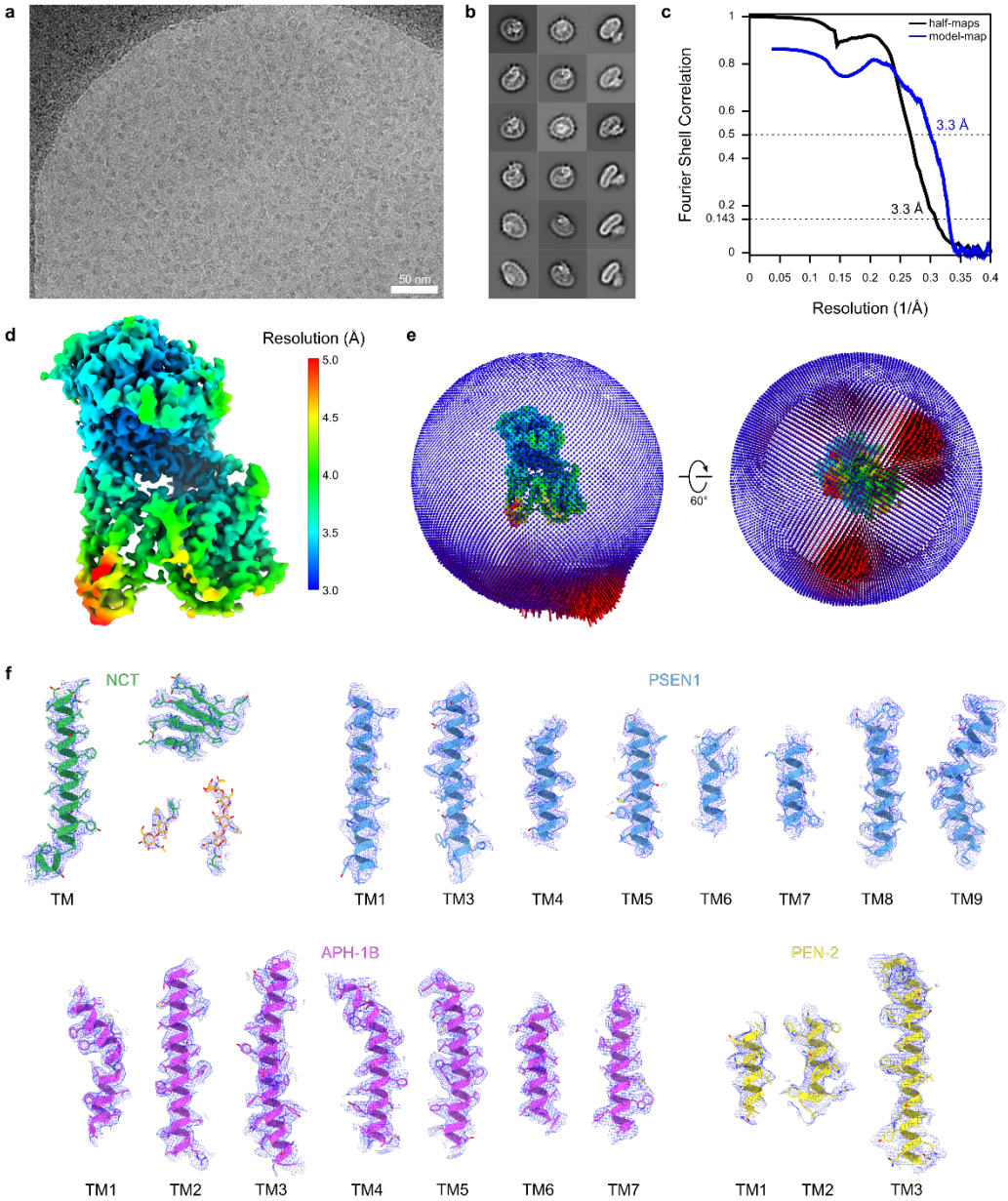


**Extended Data Figure 1. Electron microscopy and single-particle analysis of apo GSEC1B. a,** Representative micrograph from the apo GSEC1B dataset after motion correction. **b,** Example 2D class averages calculated in RELION 3.1. **c,** Masked half-map and model-map Fourier shell correlation curves. The resolution cut-offs at FSC of 0.143 and 0.5 are indicated for half-map and model-map FSCs. **d,** EM density map coloured by local resolution. **e,** Distribution of particle orientations. **f**, Examples of EM density maps (shown as mesh surfaces) around the atomic models (shown as cartoons and sticks).

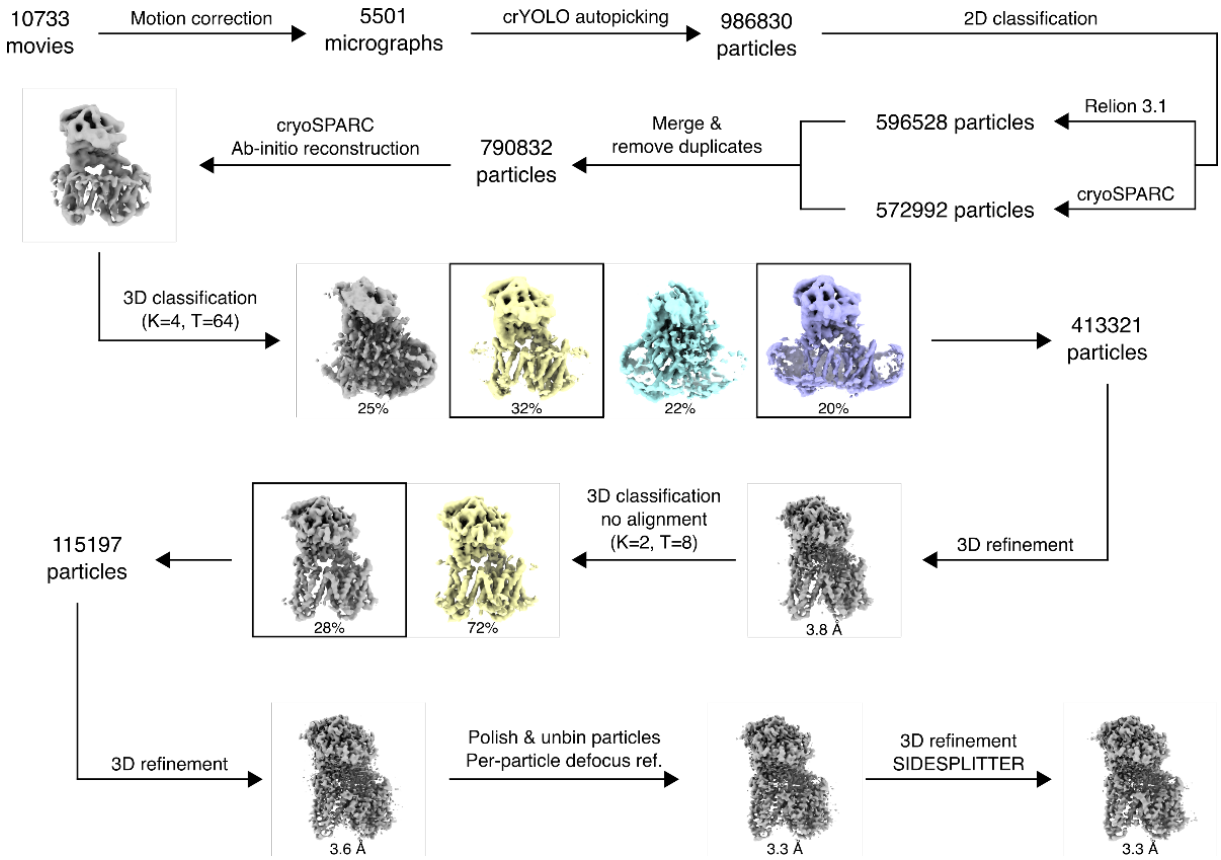


**Extended Data Figure 2. Image processing pipeline for apo GSEC1B.** Schematic representation of cryo-EM data processing procedure used for obtaining reconstruction of GSCE1B in apo form.

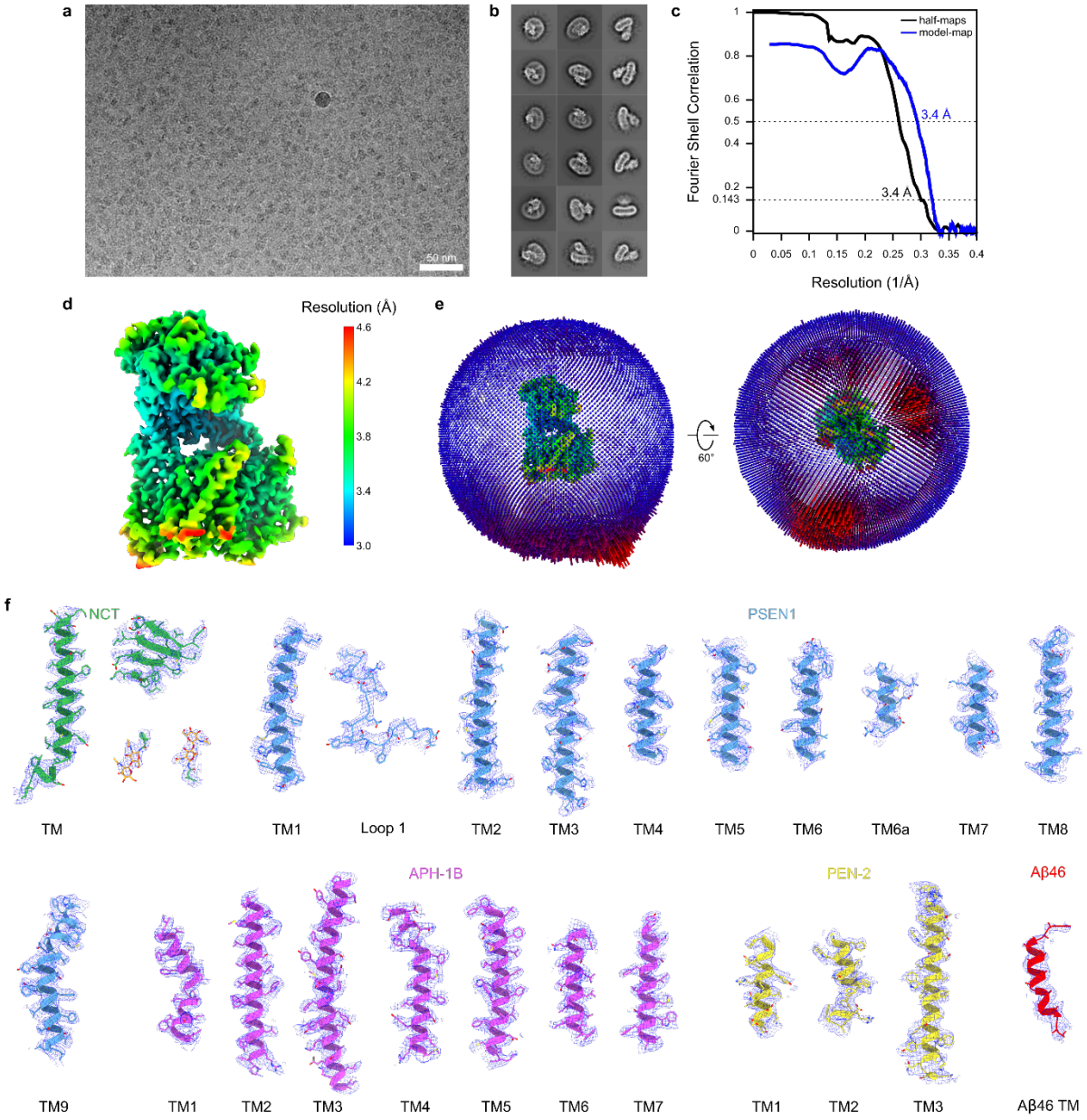


**Extended Data Figure 3. Electron microscopy and single-particle analysis of GSEC1B-Aβ46 complex. a,** Representative motion-corrected micrograph from the GSEC1B-Aβ46 dataset. **b,** Example 2D class averages calculated in RELION 3.1. **c,** Fourier shell correlation curves for masked half-maps and between model and map. The resolution cut-offs at FSC of 0.143 and 0.5 are indicated for half-map and model-map FSCs. **d,** EM density map coloured by local resolution. **e,** Distribution of particle orientations. **f**, Examples of EM density maps (shown as mesh surfaces) around atomic models (shown as cartoons and sticks).

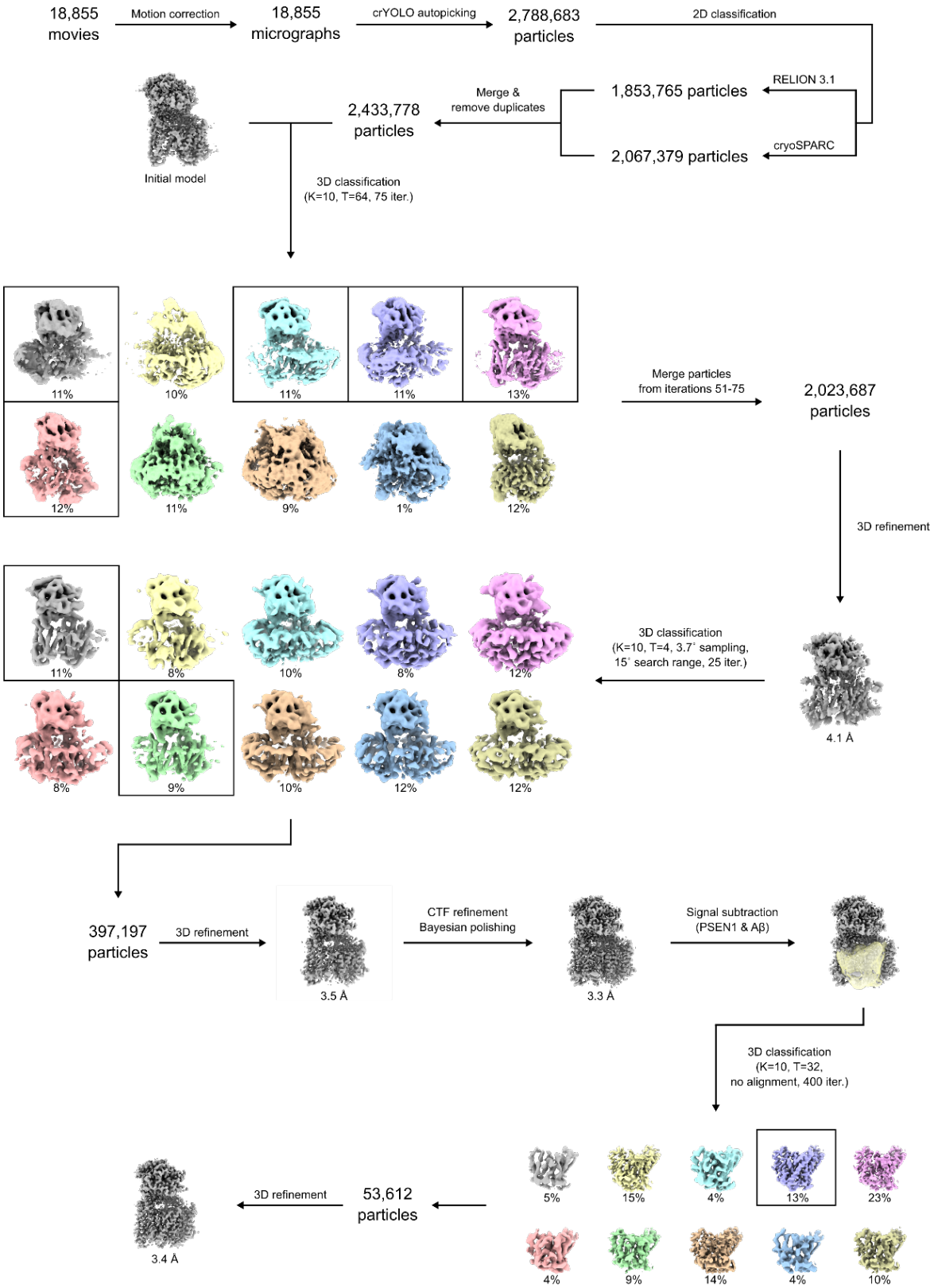


**Extended Data Figure 4. Image processing pipeline for GSEC1B-Aβ46 complex.** Schematic representation of cryo-EM data processing procedure used for obtaining reconstruction of GSCE1B-Aβ46.